Dynamics of Eddies Generated by Sea Ice Leads

KAYLIE COHANIM,[a] KEN X. ZHAO,[a] AND ANDREW L. STEWART[a]

[a] *Department of Atmospheric and Oceanic Sciences, University of California, Los Angeles, Los Angeles, California*

(Manuscript received 24 July 2020, in final form 25 May 2021)

ABSTRACT: Interaction between the atmosphere and ocean in sea ice–covered regions is largely concentrated in leads, which are long, narrow openings between sea ice floes. Refreezing and brine rejection in these leads inject salt that plays a key role in maintaining the polar halocline. The injected salt forms dense plumes that subsequently become baroclinically unstable, producing submesoscale eddies that facilitate horizontal spreading of the salt anomalies. However, it remains unclear which properties of the stratification and leads most strongly influence the vertical and horizontal spreading of lead-input salt anomalies. In this study, the spread of lead-injected buoyancy anomalies by mixed layer and eddy processes are investigated using a suite of idealized numerical simulations. The simulations are complemented by dynamical theories that predict the plume convection depth, horizontal eddy transfer coefficient, and eddy kinetic energy as functions of the ambient stratification and lead properties. It is shown that vertical penetration of buoyancy anomalies is accurately predicted by a mixed layer temperature and salinity budget until the onset of baroclinic instability (~3 days). Subsequently, these buoyancy anomalies are spread horizontally by eddies. The horizontal eddy diffusivity is accurately predicted by a mixing-length scaling, with a velocity scale set by the potential energy released by the sinking salt plume and a length scale set by the deformation radius of the ambient stratification. These findings indicate that the intermittent opening of leads can efficiently populate the polar halocline with submesoscale coherent vortices with diameters of ~10 km, and they provide a step toward parameterizing their effect on the horizontal redistribution of salinity anomalies.

KEYWORDS: Sea ice; Atmosphere-ocean interaction; Eddies; Mixing; Ocean dynamics; Oceanic mixed layer

1. Introduction

In polar regions, the exchange of mass, momentum, and heat in the atmosphere–ocean boundary layer is strongly influenced by the sea ice cover (Goosse et al. 2018; Timmermans and Marshall 2020). Sea ice cover insulates the ocean mixed layer from the atmosphere, and surface heat and salt fluxes are largely confined to gaps in the sea ice such as polynyas and leads (Smith et al. 1990; Morison et al. 1992; Ohshima et al. 2013). This study focuses on leads, which are long, narrow gaps between ice floes with widths ranging from meters to several kilometers and that last from a few hours to several days from formation to freezing (Smith et al. 1990). These openings expose the relatively warm ocean mixed layer to the polar atmosphere, leading to heat loss and refreezing at the ocean surface.

In the Arctic, the heat flux through leads is estimated to be approximately equal to the heat flux through the rest of the pack ice cover, despite composing only 1%–10% of the ice open water fraction (Smith et al. 1990; Morison et al. 1992; Smith et al. 2002). The heat flux is predominantly due to the latent heat of fusion during ice formation (since the mixed layer underneath the ice is near freezing year-round). Leads have also been shown to account for a large fraction of the total salt flux injected into the mixed layer in the Arctic (Morison et al. 1992). The salt flux is produced at the ocean surface due to brine rejection generated within the freezing lead. Parameterizing these fluxes in GCMs has been shown to be important in order to accurately simulate the Arctic stratification (Steiner et al. 2004; Nguyen et al. 2009).

The intense, localized, line-shaped buoyancy anomalies produced by leads have dynamical implications throughout the polar regions. The formation of sea ice within freezing leads creates dense convective plumes that deepen the mixed layer locally, and which can cumulatively modify the mixed layer of the entire sea ice–covered region (Smith and Morison 1998). In buoyancy-dominated regimes, such as for slow-moving leads, the resulting dense plumes penetrate the pycnocline (Smith and Morison 1998) and undergo baroclinic instability, forming submesoscale coherent vortices (SCVs) that spread lead-injected heat and salt anomalies laterally (Bush and Woods 1999; Marshall and Schott 1999; Smith et al. 2002).

In the Arctic, previous studies have observed anticyclonic eddies with cold/high-salinity cores near the pycnocline, and horizontal scales of 10–20 km (D'Asaro 1988; Muench et al. 2000; Timmermans et al. 2008; Zhao et al. 2014, 2016). Depending on their origin, it has been suggested that these eddies can be generated by instabilities in the shelf break or coastal currents (D'Asaro 1988; Manley and Hunkins 1985; Pickart et al. 2005). Timmermans et al. (2008) showed that eddies observed in the central Canada Basin can be generated by the instabilities in upper-ocean fronts, and are capable of propagating far from their origin front (Manucharyan and Timmermans 2013). Previous laboratory and idealized modeling studies have found that lead openings produce much smaller eddies (typically a few kilometers in diameter), and suggested that such eddies would be quickly dissipated, rather than contributing to the under-sea-ice eddy field (Bush and Woods 1999, 2000; Smith et al. 2002; Matsumura and Hasumi 2008).

Much less is known about the presence of SCVs under Antarctic sea ice and about their relation to the opening leads.

Corresponding author: Kaylie Cohanim, kcohanim@princeton.edu

DOI: 10.1175/JPO-D-20-0169.1

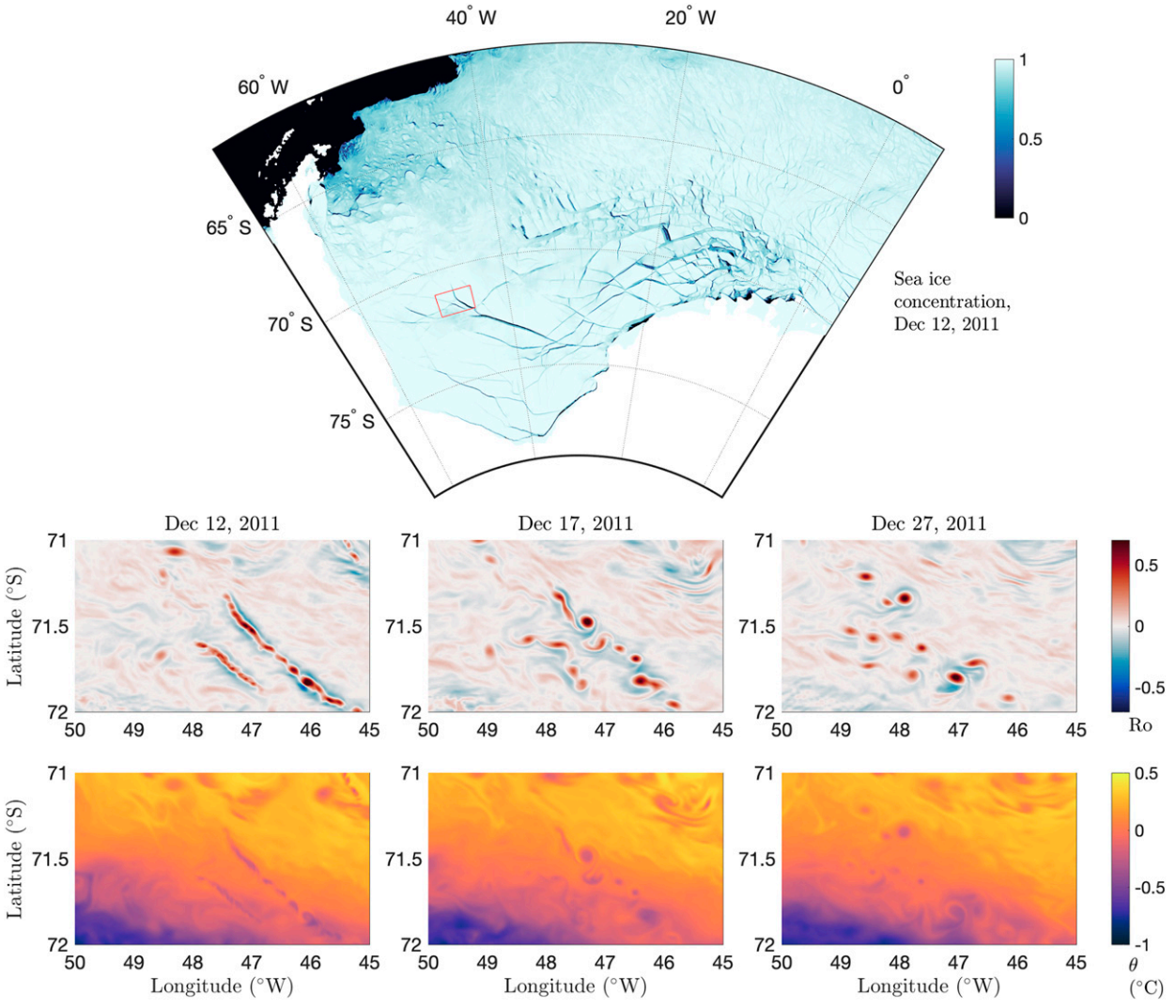

FIG. 1. An example of a lead eddy generation event from a high-resolution global ocean/sea ice simulation. (top) Daily-averaged sea ice concentration on 12 Dec 2011 in the Weddell Sea sector of the LLC4320 simulation (see Stewart et al. 2018, 2019), and snapshots of (middle) relative vorticity normalized by the local Coriolis parameter and (bottom) potential temperature. These snapshots span the area indicated by the red-outlined box in the top panel, at a depth of 352 m.

Some insight may be gained from high-resolution models, such as the one illustrated in Fig. 1. This simulation was run globally at 1/48° (~1-km grid spacing in polar regions) using the MIT general circulation model (MITgcm) and is described in more detail by Rocha et al. (2016) and Stewart et al. (2019). Figure 1 shows a Weddell Sea that is populated by many SCVs with diameters of a few tens of kilometers in this model. This figure highlights a specific lead opening event in the southern Weddell Sea, which produces localized convection and a chain of anticyclonic eddies. This mechanism is consistent with previous laboratory experiments (Bush and Woods 1999, 2000) and idealized modeling studies (Smith et al. 2002; Matsumura and Hasumi 2008). However, these eddies occur much deeper (hundreds of meters below the surface) and have consistently larger diameters (~10 km) than indicated by previous studies. This suggests that such lead opening events might play a key role in sustaining the eddy field under sea ice. A caveat to investigating the formation of eddies in such models is that even at this fine grid resolution only the largest leads, with widths of several km or more, are resolved.

Many gaps in understanding currently remain with respect to lead-generated eddies. In particular, although previous studies have shown that lead eddies spread lead-injected buoyancy anomalies horizontally (Bush and Woods 1999, 2000; Send and Marshall 1995; Matsumura and Hasumi 2008), the length and time scales over which this spread occurs have yet to be quantitatively linked to the properties of the lead and the ambient ocean stratification. Furthermore, while eddy formation beneath the lead has been shown to hinder deepening of the surface mixed layer due to surface buoyancy loss within the lead (Matsumura and Hasumi 2008), a quantitative understanding of this relationship has not yet been established.

Previous studies have also not addressed the role of frictional drag against the overlying sea ice in the formation, spread, and longevity of under-lead eddies. Additionally, it remains unclear whether lead-injected buoyancy anomalies are capable of producing larger (tens of kilometers wide) eddies that are sufficiently long-lived to transport buoyancy anomalies over long distances and populate the Arctic and Antarctic polar pycnoclines.

In this study, we use an idealized numerical model with supporting dynamical theories/scalings to investigate the role of lead eddies in mediating the vertical and horizontal spread of lead-injected buoyancy anomalies and their potential contribution to the polar eddy field. The motivation behind this is to extend our current understanding of lead-generated eddy dynamics and assess their potential impact on the stratification and circulation of ice-covered region, with a particular emphasis on the Antarctic margins. The structure of this article is as follows. In section 2, we present the idealized MITgcm model configuration and the rationale behind our choices of parameters and the parameter space explored. In section 3, we discuss a reference simulation to illustrate the phenomenology of eddy formation beneath leads. We also introduce key metrics of eddy-mediated spread of buoyancy anomalies and of the eddies themselves: the mixed layer depth (MLD) deepening, the lateral buoyancy diffusivity κ, and the eddy size D. In section 4, we investigate the dependencies of the MLD, κ, and D on key lead and stratification parameters: the initial MLD, the pycnocline thickness, the atmospheric temperature, the lead width, the vertical temperature and salinity gradients, and the sea ice drag coefficient. In section 5, we present theoretical predictions for the MLD, κ, and D and evaluate these theories against our simulation results. In section 6, we summarize our results and provide concluding remarks.

2. Modeling approach

Because lead eddies may play a part in the dynamics of any ice-covered region, we seek to construct a model that represents a range of regional and seasonal profiles characteristic of ice-covered oceans that can be applied both to the Arctic and Antarctic. To allow for such flexibility, we construct a model to permit variations in the ambient ocean stratification, the surface buoyancy forcing, the sea ice drag, and the width of the lead itself. In section 2a, we introduce the model configuration used and explain the rationale behind the chosen parameters. In section 2b, we introduce a reference simulation that will be explored in section 3.

a. Model configuration

We implement a model configuration representative of sea ice covered regions with an idealized lead. Lead dimensions can vary greatly, spanning hundreds of meters to several kilometers wide and tens to hundreds of kilometers long (Smith et al. 1990). Furthermore, sonar data from the Davis Strait indicate that the spacing between leads of ~1 km in width varies from ~5 km near the marginal ice zone to ~30 km in interior ice regions. These separation distances increase with greater lead widths (Wadhams et al. 1985). An additional constraint on our model is that the horizontal resolution should sufficiently resolve convection and the eddy formation process beneath the lead. To balance these requirements against the computational cost, we use a domain size of $L_x \times L_y \times H = 50\,\text{km} \times 50\,\text{km} \times 500\,\text{m}$, a uniform horizontal resolution of $\Delta x = \Delta y = 125\,\text{m}$, and a uniform vertical resolution of $\Delta z = 5\,\text{m}$. Our model therefore spans a larger area than previous comparable modeling studies, within a finer grid spacing (e.g., Smith et al. 2002; Matsumura and Hasumi 2008).

We use the MIT general circulation model (MITgcm; Marshall et al. 1997a,b) to solve the nonhydrostatic Boussinesq equations on an f plane (Vallis 2006). We evolve both potential temperature and salinity, which are related to in situ density using the equation of state of Jackett and McDougall (1995). We use doubly periodic horizontal boundary conditions, with a single lead centered at $y = 0$ (see Figs. 2 and 3). Thus, the lead is effectively separated from identical, parallel leads by 50 km in the y direction. We use a free-slip flat bottom boundary $z = -500\,\text{m}$ and impose a rigid lid at the upper boundary $z = 0$. We impose a grid-dependent horizontal biharmonic viscosity in a Laplacian vertical viscosity to control gridscale accumulation of energy and enstrophy, and we use a flux-limited third-order discrete space–time scheme to advect potential temperature and salinity.

We prescribe initial conditions of zero velocity and a horizontally uniform potential temperature and salinity stratification composed of a surface mixed layer overlying a pycnocline, with weak stratification below the pycnocline (see Fig. 2). Specifically, we set $S = S_0(z)$ and $\theta = \theta_0(z)$, where

$$S_0(z) = S_{\text{min}} + \frac{\Delta S}{2}\left[1 + \frac{\Gamma(\tilde{z})}{2}\right] \quad \text{and} \tag{1a}$$

$$\theta_0(z) = \theta_f + \frac{\Delta\theta}{2}\left[1 + \frac{\Gamma(\tilde{z})}{2}\right]. \tag{1b}$$

Here $\tilde{z} = [z + (H_0 + H_{\text{pyc}}/2)]/H_{\text{pyc}}$ is a normalized vertical coordinate that is equal to zero in the middle of the pycnocline, $z = -H_0 + H_{\text{pyc}}/2$, with H_0 being the initial mixed layer thickness and H_{pyc} being the pycnocline thickness. The vertical structure function

$$\Gamma(\tilde{z}) = \frac{\sqrt{(1-\tilde{z})^2 + 4\gamma\tilde{z}^2} - \sqrt{(1+\tilde{z})^2 + 4\gamma\tilde{z}^2}}{\sqrt{1+\gamma}}, \tag{2}$$

with steepness parameter $\gamma = 0.01$, produces an approximately piecewise-linear stratification, and is plotted in Fig. 2a. The parameters $\Delta S = S_{\text{max}} - S_{\text{min}}$ and $\Delta\theta = \theta_{\text{max}} - \theta_{\text{min}}$ define the total changes in potential temperature and salinity across the pycnocline, respectively. The surface temperature is set to the surface freezing temperature, calculated using $\theta_f = 0.0901 - 0.0575 S_{\text{min}}$ (Millero and Leung 1976). All of our simulations are initialized from this prescribed stratification, with varying H_0, H_{pyc}, $\Delta\theta$, and ΔS. Each experiment is integrated for a total of 50 days, by which time the lead-input buoyancy anomalies typically reach the northern and southern domain boundaries.

The model is forced at the surface by parameterized growth of ice within a lead of width W, and the flow is damped by a parameterized stress between the ocean and the overlying sea ice, which is assumed to be stationary for simplicity. We do not attempt to simulate sea ice growth and dynamics explicitly

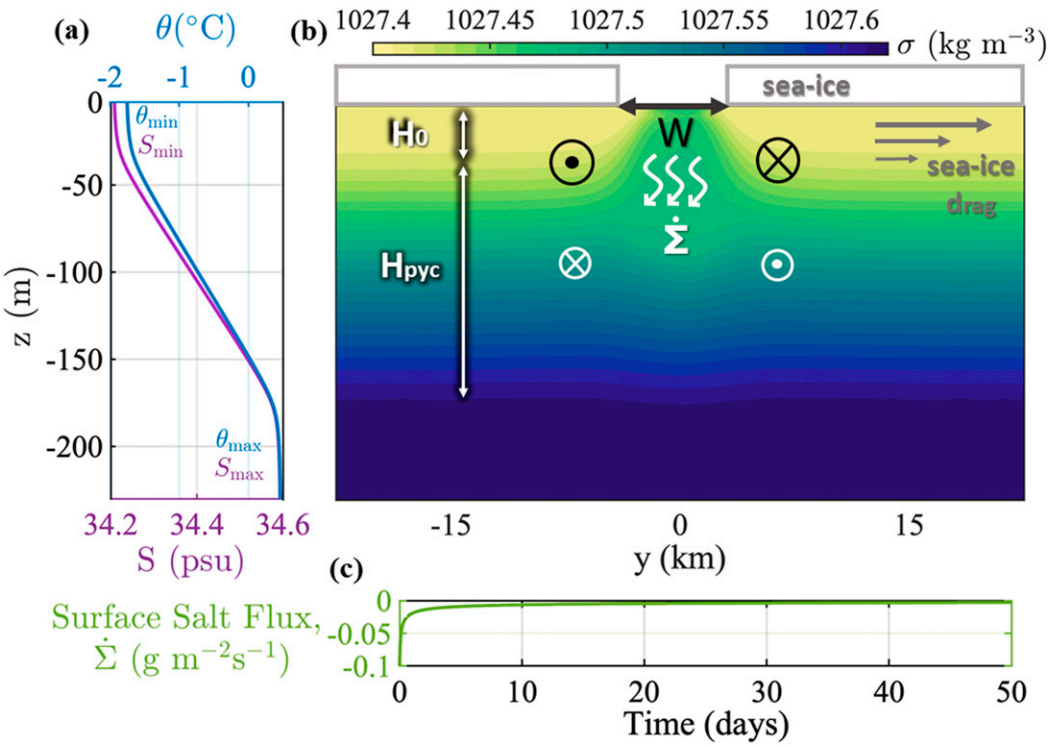

FIG. 2. Schematic of the model setup for our reference simulation (see section 2b). (a) Initial potential temperature and salinity profiles, with maximum and minimum potential temperatures and salinities indicated. (b) Schematic of the model forcing and lead convection process. Colored contours show the along-lead-averaged potential density field on day 10 of our reference simulation, at intervals of 0.01 kg m^{-3}. Key model parameters are sketched: the initial mixed layer thickness H_0, the pycnocline thickness H_{pyc}, the lead width W, and the surface salt flux $\dot{\Sigma}$. (c) Time evolution of the imposed upward surface salt flux in the lead, per unit area.

because this would introduce substantial additional complexity to the model (Semtner 1976; Hibler 1979), and our focus is on the oceanic response. We therefore prescribe a time-dependent salt flux $\dot{\Sigma}(t)$ following Anderson (1961) that is uniform across the width of the lead and depends only on a specified atmosphere–ocean temperature difference parameter T_{atm}. Figure 2c shows this salt flux as a function of time in our reference simulation. We additionally assume that any heat anomalies that reach the surface within the lead are immediately removed by air–ice–ocean interactions, which we represent by restoring the potential temperature to the freezing temperature in the surface grid boxes over a time scale of one day. We represent ocean–sea ice drag mechanical stresses via a linear drag, with drag velocity r_b that is applied across the entire surface of the model domain.

This model setup allows both 2D and 3D configurations, which allows us to compare experiments with eddies (in the 3D cases) and without eddies (in the 2D cases), which we discuss in section 3. The 2D and 3D configurations differ from one another only in the number of grid points: a single grid point is used in the x direction to run the model in 2D.

b. Reference case

Previous studies about lead-generated eddies have primarily focused on the Arctic (Smith et al. 2002; Matsumura and Hasumi 2008). However, conditions surrounding Antarctica may be more or less favorable for the genesis and longevity of lead eddies due to its deeper pycnocline and colder atmospheric forcing, which motivates us to design a model configuration that is representative of the Antarctic. We specifically target the Weddell Sea, because the global high-resolution model discussed in section 1 simulates an abundance of under-sea-ice SCVs in this region (see Fig. 1). The latitude is therefore set at 70°S with a Coriolis parameter $f_0 = -1.375 \times 10^{-4}\,\text{s}^{-1}$.

We select our reference case on the basis of the analysis of measurements from 2859 CTD profiles deployed in the Weddell Sea continental slope (Hattermann 2018). The analysis provides the temperature and salinity profiles both onshore and 100 km offshore between 1977 and 2016. We choose to favor offshore conditions because this choice better reflects the majority of the region, as well as conditions that are better representative of all months of the year and not a specific season.

From these profiles, we select reference parameter values of $S_{\text{max}} = 34.6$ psu, $S_{\text{min}} = 34.2$ psu, $\theta_{\text{max}} = 0.5$°C, $H_0 = -30$ m, and $H_{\text{pyc}} = 150$ m. The freezing temperature is calculated using S_{min}, such that $\theta_f \approx -1.9$°C. This value is comparable to the typical temperatures observed in the Antarctic (Turner et al. 2005). The atmosphere–ocean temperature difference is set to $T_{\text{atm}} = -25$°C, as Antarctic atmospheric temperatures typically range from −10° to −40°C. We use an ocean–sea ice drag velocity of $r_b = 2.5 \times 10^{-4}\,\text{m s}^{-1}$, which is approximately

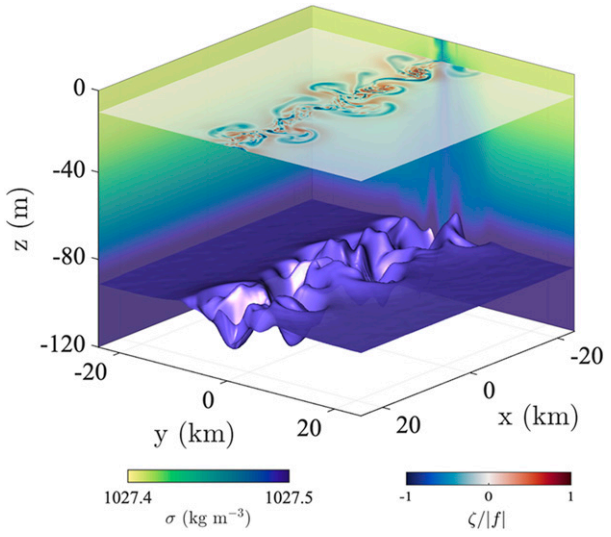

FIG. 3. A 3D rendering of a snapshot from day 10 of our reference simulation (see Table 1). The upper horizontal slice shows relative vorticity, normalized by the Coriolis parameter, at $z = -12.5$ m. The undulating purple curve corresponds to the 1027.5 kg m^{-3} potential density surface, which lies within the pycnocline. Background shading shows slices of the instantaneous potential density field along $y = -25$ km and $x = -25$ km.

consistent with a quadratic ice–ocean drag coefficient of $C_{io} \approx 5 \times 10^{-3}$ and surface ice–ocean shear of 0.05 m s^{-1} (Cole et al. 2014). While previous studies typically focus on lead widths smaller than 1 km, our focus here is on the wider leads, which produce greater heat and salt fluxes. These leads are therefore more likely to influence the ocean mixed layer as well as favor the growth of maintenance of long-lived lead-generated eddies. Thus, we set a reference case lead width of $W = 3$ km, as typical observed lead width for these scales range between 2 and 4 km (Key et al. 1993). The parameters used in our reference simulation are listed in Table 1.

A snapshot of the 3D reference simulation at $t = 10$ days is shown in Fig. 3. The background shadings show the density field at $x = -25$ km and $y = -25$ km, displaying a plume generated by buoyancy fluxes at the surface (Fig. 2c) and sinking to levels of $z \approx -85$ m. The bottom undulating purple curve corresponds to the 1027.5 kg m^{-3} potential density surface, and the upper horizontal slice shows the vorticity field right below the lead surface ($z = -12.5$ m), both illustrating the relationship between the lead buoyancy forcing and the resulting generation and horizontal spread of the eddy field.

3. Phenomenology of lead eddy formation

In this section, we briefly describe the formation and phenomenology of lead eddies in our reference case, which is discussed in more detail in previous studies (Bush and Woods 1999; Smith et al. 2002; Matsumura and Hasumi 2008). We then describe our approach for quantifying specific properties of the eddies and the spread of lead-input buoyancy anomalies.

TABLE 1. List of parameters used in the reference model run. Italics indicate parameters that are independently varied between model runs.

	Value	Description
L_x	50 km	Zonal domain size
L_y	50 km	Meridional domain size
H	500 m	Domain depth
Δx	125 m	Zonal grid spacing
Δy	125 m	Meridional grid spacing
Δz	5 m	Vertical level spacing
Δt	49 s	Time-step size
t_s	50 days	No. of simulated days
W	3 km	*Width of lead*
H_0	30 m	*Initial mixed layer depth*
H_{pyc}	150 m	*Initial pycnocline thickness*
θ_f	−1.9°C	Freezing temperature
θ_{max}	0.5°C	*Max temperature*
S_{min}	34.2 psu	Min salinity
S_{max}	34.6 psu	*Max salinity*
T_{atm}	−25°C	*Atmospheric temperature*
r_b	2.5×10^{-4} m s^{-1}	*Ice drag velocity*
ρ_0	1027 kg m^{-3}	Reference saltwater density
ρ_i	920 kg m^{-3}	Density of ice
S_i	5 psu	Salinity of ice
g	9.81 m^2 s^{-1}	Gravitational constant
f_0	-1.375×10^{-4} s^{-1}	Coriolis parameter
$A_{4,grid}$	0.2	Grid-dependent biharmonic viscosity
A_r	1×10^{-3} m s^{-2}	Vertical Laplacian viscosity

a. Lead eddy formation and phenomenology

The formation of lead eddies begins with the buoyancy loss due to freezing of the ocean surface layer, resulting in a convective plume (Figs. 2b and 3). Mixing within this plume creates a deeper and denser mixed layer beneath the lead. The mixed layer deepens until it reaches its level of neutral buoyancy and then spreads these buoyancy anomalies horizontally. This process is particularly clear in the 2D simulations (right column) of Fig. 4, which compares the evolution of 2D and 3D along-lead averaged density fields at $t = [1, 3, 5, 10, 30, 50]$ days. In contrast to the 2D simulations, the convective plume in the 3D (left column) stops deepening around day 3. This suggests that the deepening of the mixed layer is arrested by the genesis of eddies, which cannot form in the 2D simulations.

As the mixed layer becomes deeper and denser it forms a filament that geostrophically adjusts, occurring approximately over an inertial time scale. This leads to the formation of along-lead jets (see, e.g., Matsumura and Hasumi 2008), as illustrated in Fig. 2b. The jets are associated with vorticity anomalies: at the base of the mixed layer positive vorticity occurs within the filament and negative vorticity occurs along the outer edges of the filament (Fig. 5a). This structure is baroclinically unstable, leading to the formation of eddies (Figs. 5b,c). The eddies then begin to interact and merge with one another, growing continually until the end of the simulation (Figs. 5d,f). Throughout the evolution, anticyclonic vortices dominate, consistent with Fig. 1 and previous studies (e.g., Bush and Woods 1999).

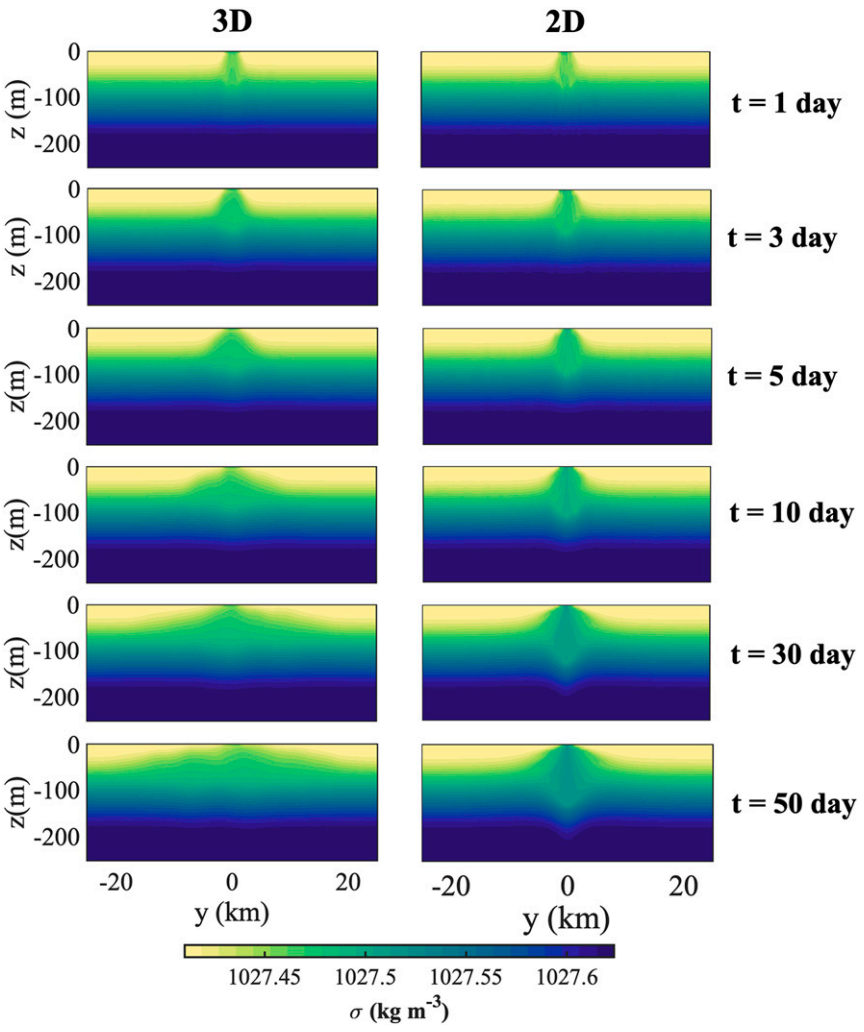

FIG. 4. Evolution of the density field with and without the action of eddies. Panels show snapshots of the along-lead-averaged potential density fields in (left) three-dimensional and (right) two-dimensional reference simulations at days 1, 3, 5, 10, 30, and 50. Contour intervals are 0.01 kg m^{-3}.

Figure 4 also shows the impact of the growth and spread of eddies via the evolution of the cross-lead density field. In the 2D simulation, the lead-driven buoyancy anomalies are confined to within a few km of the lead itself, while in the 3D simulation, the horizontal spread of the buoyancy anomalies is substantially enhanced and is visible as early as day 5. By day 50, the lead-input buoyancy anomalies have modified the upper-ocean stratification across the entire model domain. Specifically, outside of the below-lead region, buoyancy anomalies spread as a layer of thickness 50–100 m, centered around a depth of approximately 70 m. The stratification of this layer is stronger than that of the initial mixed layer, but weaker than that of the initial pycnocline stratification.

To summarize, buoyancy loss within the lead serves to deepen the mixed layer locally, but this deepening appears to be arrested after a few days. Thereafter, the baroclinic growth and spread of eddies serves to spread buoyancy anomalies primarily in the horizontal, rather than the vertical.

b. *Lead eddy diagnostics and properties*

We now aim to quantify key properties of lead-generated eddies and their impact on the upper-ocean stratification. These properties will serve as the basis of our model parameter exploration in section 4 and the development of our scalings in section 5. Specifically, we quantify the vertical and horizontal penetration of lead-input buoyancy anomalies via the mixed layer depth and the horizontal eddy diffusivity, respectively, and we quantify the dominant length scale of the eddies. The mixed layer depth and eddy diffusivity quantify the effect of leads and eddies on the upper-ocean stratification in the polar regions, while the eddy size provides an indication of the potential contribution of lead eddies to the eddy field in sea ice–covered regions. Another motivation for quantifying these

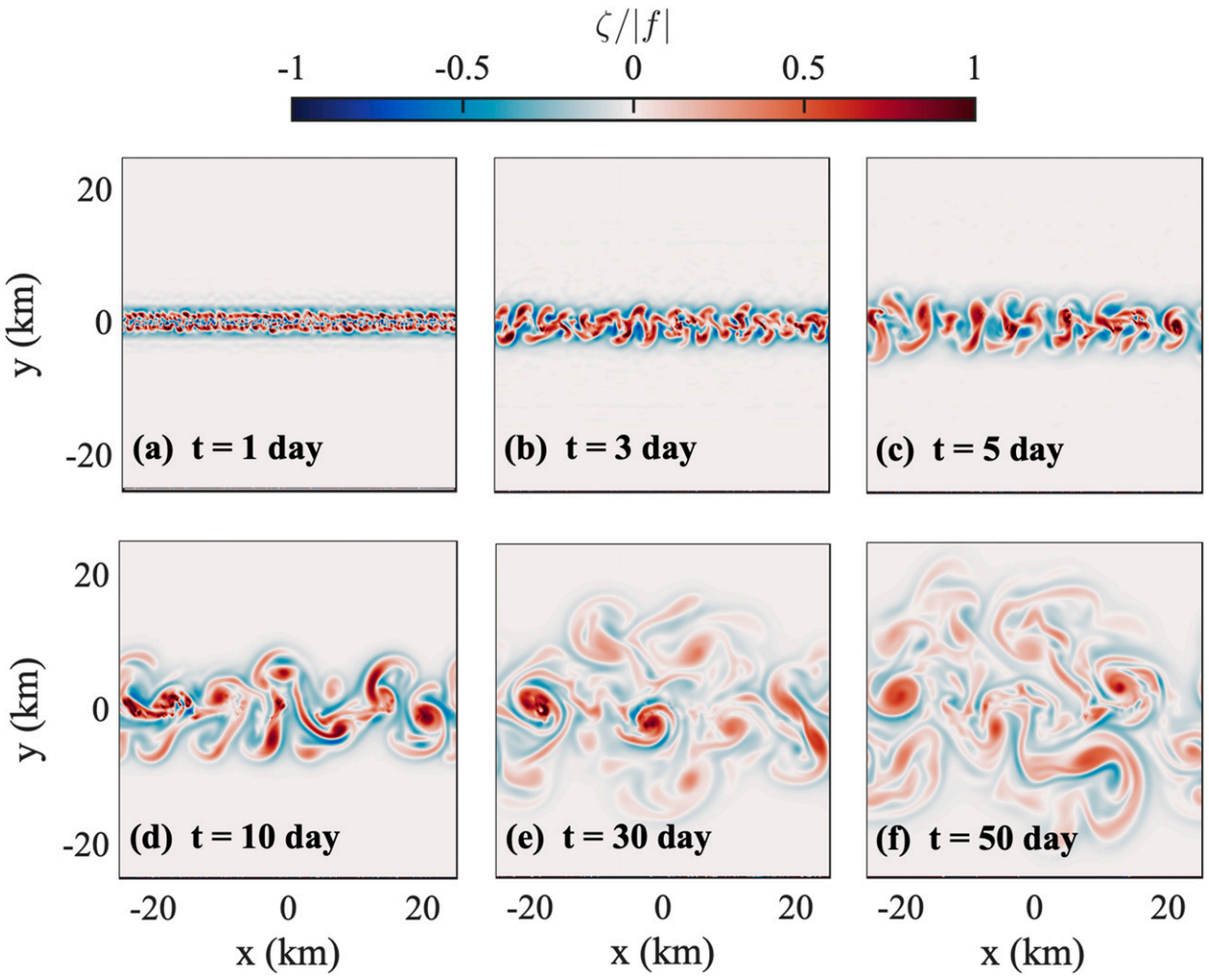

FIG. 5. Evolution of the eddy field, showing snapshots of the relative vorticity field, normalized by the Coriolis parameter, at the mixed layer depth of $z \approx -85$ m in our reference simulation.

properties is they are all amenable to direct observational estimates, e.g., via hydrographic sampling.

1) MIXED LAYER DEPTH

Various previous algorithms have been proposed to diagnose MLDs from hydrographic measurements (e.g., Holte and Talley 2009). However, the simplified initial θ and S profiles imposed in our simulations (see section 2) allow us to tailor a more specific algorithm. Specifically, we find the MLD using the first inflection point of the density profile beneath the lead starting from the surface; that is,

$$\left.\frac{\partial^2 \overline{\sigma}^{x,W}}{\partial z^2}\right|_{z=z_{\mathrm{ML}}} = 0 \quad \text{for} \quad z_{\mathrm{ML}} < -25\,\mathrm{m}. \tag{3}$$

Here $\overline{\sigma}^{x,W}$ denotes the potential density averaged over the entire lead area. To find the inflection point, we interpolate σ vertically to a finer vertical resolution (0.1 m) using cubic splines, and then compute the discrete second derivative of the potential density in Eq. (3). The density profile above $z = -25$ m is excluded because it typically contains a density inversion associated with convection within the lead.

In Fig. 6a, we plot profiles of $\overline{\sigma}^{x,W}$ from our 2D and 3D reference simulations at $t = 0$, $t = 3$, and $t = 50$ days and indicate the MLDs diagnosed using Eq. (3). The results demonstrate that the method successfully diagnoses the MLD throughout the evolution of the simulation. We also tested density threshold and density gradient threshold-based quantifications of the MLD (see Holte and Talley 2009). While these methods produce quantitatively very similar estimates of the MLD in our reference simulation, we found that they did not generalize accurately across our sensitivity experiments (see section 4).

To further examine the 2D and 3D MLD evolution, we plotted the diagnosed MLD within the lead as a function of time in Fig. 6b. Comparing the 2D and 3D simulations allows us to disentangle the effects of the surface buoyancy fluxes from the onset of baroclinic instabilities on MLD. Notice that the 3D case does not exhibit any significant trend after

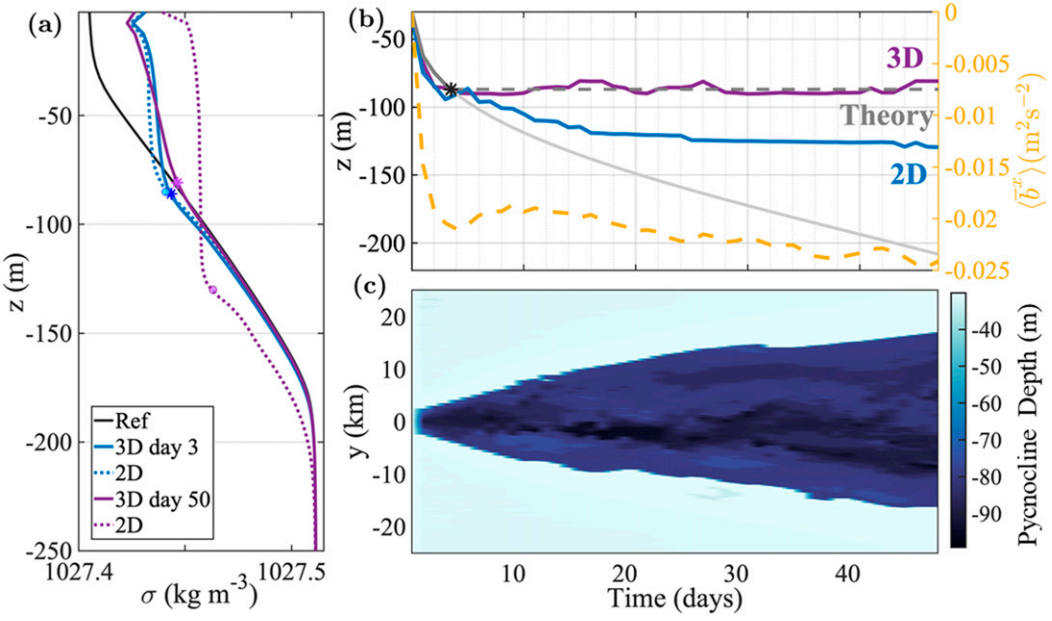

FIG. 6. Diagnostics of the MLD in our reference simulation (see Table 1). (a) Lead-averaged potential density profiles from 3D (solid line) and 2D (dotted line) simulations at $t = 3$ days and $t = 50$ days. Asterisks and circles indicate the diagnosed MLDs for the 3D and 2D case, respectively. (b) Evolution of the MLD, computed using the along- and across-lead averaged density field, in our 3D and 2D reference simulations, and as predicted by our theory (see section 5). Also shown is the depth-integrated buoyancy anomaly in the 3D case, $\langle \overline{b}^x \rangle$, averaged over the lead. (c) Evolution of the pycnocline depth in the 3D case, computed using the along-lead averaged density field, as a function of cross-lead distance.

$t \sim 4$ days. On the other hand, there is a significant trend in the 2D case; between days 4 and 25, the plume depth approximately doubles. Thus, the 2D and 3D cases are not only qualitatively different, but their quantitative differences are substantial. These results are consistent with our qualitative inferences from Fig. 4 in section 3a: the deepening of the mixed layer halts after a few days in the 3D simulation but persists and weakens with time in the 2D simulation, suggesting that ML deepening is arrested via the genesis of eddies.

In Fig. 6c, we plot the evolution of the depth diagnosed via Eq. (3) as a function of both cross-lead distance and time for the 3D reference case. Outside the lead we refer to this depth as the pycnocline depth, as the waters above this depth are not generally well mixed (see Fig. 4): the vertically averaged buoyancy frequencies inside and outside the lead are $N = 0.0026\,\mathrm{s}^{-1}$ and $N = 0.0032\,\mathrm{s}^{-1}$, respectively. The pycnocline depth is determined at each point in y using the potential density from Eq. (3) but averaged only in the x direction rather than over the entire lead. Figure 6c shows that the horizontal spread of weakly stratified waters from the lead, visible in Fig. 4, is associated with a substantial deepening of the pycnocline depth across an increasingly wide span of the model domain. By the end of the simulation ($t = 50$ days), the shallow well-mixed layer is replaced with a deep weakly stratified layer, extending 10–20 km in either direction perpendicular to the lead. Thus, via the action of the eddies, the lead-input buoyancy anomalies substantially alter the upper-ocean stratification over an area many times the size of the lead itself. Potential implications of this effect for ice-covered regions of the ocean are discussed in section 6.

2) EDDY DIFFUSIVITY

Figure 4 illustrates the horizontal spread of lead-input buoyancy anomalies due to lead eddies, while Fig. 6c shows their impact on the pycnocline depth in the vicinity of the lead. We now quantify this horizontal spread using the depth-integrated buoyancy anomaly $\langle \overline{b}^x \rangle$, where the angle brackets denote a vertical integral,

$$\langle \overline{b}^x \rangle = \frac{1}{L_x} \int_0^{L_x} dx \int_{-H}^{0} dz\, b. \tag{4}$$

Here b ($\mathrm{m\,s^{-2}}$) is the buoyancy anomaly,

$$b = -g \frac{\rho - \rho|_{t=0}}{\rho_{\mathrm{ref}}}, \tag{5}$$

where g is gravity, ρ is density, and $\rho_{\mathrm{ref}} = 1027\,\mathrm{kg\,m^{-3}}$ is the reference density. Figure 6b shows the evolution of $\langle \overline{b}^x \rangle$, averaged over the lead, as a function of time, and shows that buoyancy anomalies stop accumulating in the lead around the same time as the ML stops deepening. We plot the evolution of $\langle \overline{b}^x \rangle$ as a function of time and cross-lead distance in Fig. 7a, visualizing the spread of buoyancy anomalies away from the lead. This is consistent with our previous inferences that lead eddies spread buoyancy anomalies horizontally, based on Figs. 4 and 5.

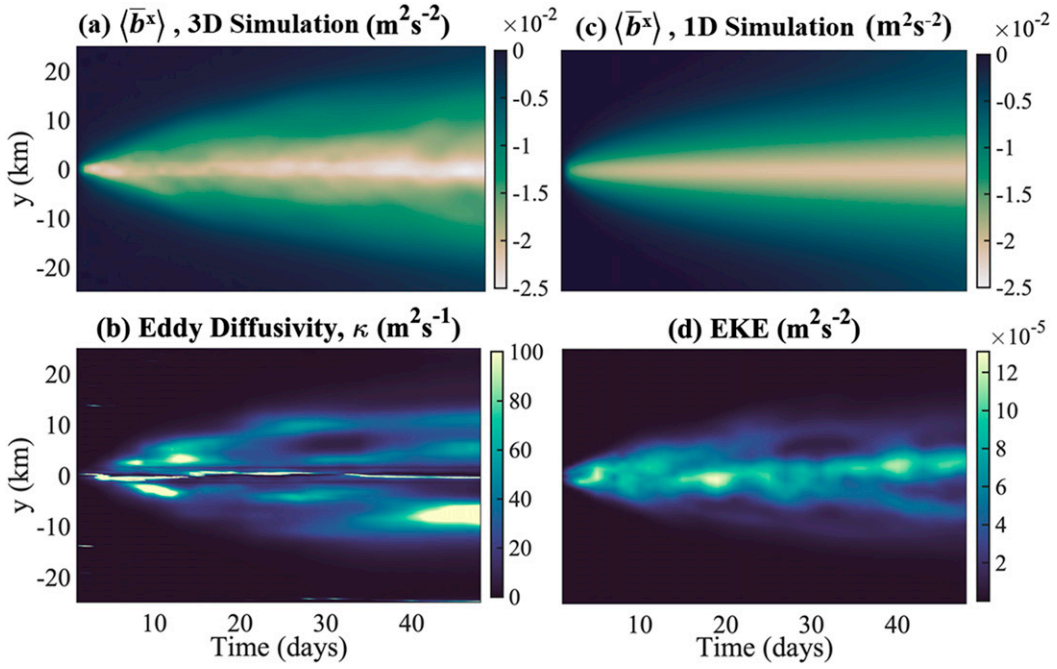

FIG. 7. Temporal and cross-lead evolution of lead-input buoyancy anomalies and eddy activity. (a) Depth-integrated and along-lead-averaged buoyancy anomalies in our 3D model reference simulation. (b) Eddy diffusivity computed from our 3D model reference simulation, following temporal smoothing of the buoyancy gradients and eddy buoyancy fluxes (see section 3a). (c) As in (a), but derived from our 1D model (see section 3b) using a bulk eddy diffusivity $\kappa_\ell = 29.1$. (d) Depth-averaged eddy kinetic energy in our 3D model reference simulation.

To quantify the rate of this horizontal spread, we define an eddy diffusivity. We start by writing an equation for the evolution of $\langle \overline{b}^x \rangle$; under the assumption that the buoyancy anomaly is materially conserved, it may be shown that

$$\frac{\partial \langle \overline{b}^x \rangle}{\partial t} = -\frac{\partial}{\partial y}\langle \overline{v' b'^x} \rangle + \dot{\overline{B}}^x. \tag{6}$$

Here primes denote deviations from the along-lead average and vertical integral—for example, $b' \equiv b - \langle \overline{b}^x \rangle$, and $\dot{B}$ is the downward surface buoyancy flux with units of meters squared per seconds cubed. To derive Eq. (6) we have used the fact that $\langle \overline{v}^x \rangle = 0$, by volume conservation. This equation states that the along-lead averaged and depth-integrated buoyancy anomaly changes in response to buoyancy fluxes across the ocean surface and in response to cross-lead eddy buoyancy fluxes, $\langle \overline{v' b'^x} \rangle$. We can model these eddy buoyancy fluxes based on the along-lead averaged and depth-integrated buoyancy anomalies using a Fickian diffusion,

$$\langle \overline{v' b'^x} \rangle = -\kappa \frac{\partial \langle \overline{b}^x \rangle}{\partial y}, \tag{7}$$

where κ is the eddy diffusivity. This formulation is consistent with the spreading of buoyancy anomalies shown in Fig. 7a, and with widely used parameterizations of mesoscale (Gent and McWilliams 1990) and submesoscale (Fox-Kemper et al. 2008) eddies in ocean general circulation models.

In Fig. 7b, we plot κ computed directly from our 3D reference simulation as a function of time and across-lead distance. To avoid very large spikes in the diffusivity for the purposes of this plot, we have performed a running time-average of both $\overline{v' b'^x}$ and $\langle \overline{b}^x \rangle$ before using these quantities to calculate κ via Eq. (7). We varied the length of the time-averaging window from 1 day at t = 0–10 days to 10 days at t = 20–50 days to ensure that the time-averaging window consistently spanned multiple eddy turnover time scales. Despite this additional smoothing, the diagnosed κ remains noisy, with values ranging over an order of magnitude, from 10 to over 100 $\mathrm{m^2\,s^{-1}}$. This pronounced spatiotemporal variability is linked to variability in the locations and circulations of the eddies, as shown in Fig. 7d. Here, we plot the depth-averaged eddy kinetic energy (EKE), which is defined as

$$\mathrm{EKE} = \frac{1}{2}\left(\overline{u^{\dagger 2}}^x + \overline{v^{\dagger 2}}^x\right) \tag{8}$$

where u and v are the horizontal velocity components and daggers denote deviations from the zonal mean; for example, $u^\dagger = u - \overline{u}^x$. We discuss the relationship of the κ with EKE further in section 5b.

The high spatiotemporal variability of κ diagnosed using Eq. (7) hinders intercomparison between simulations, for example in our parameter sensitivity experiments (see section 4). We therefore instead derive a bulk estimate of the eddy diffusivity κ_ℓ that is spatially and temporally uniform. For a one-dimensional tracer spreading unidimensionally from a release point, analogous to the spreading of depth-integrated buoyancy anomalies in Fig. 7, the tracer may be expected to spread

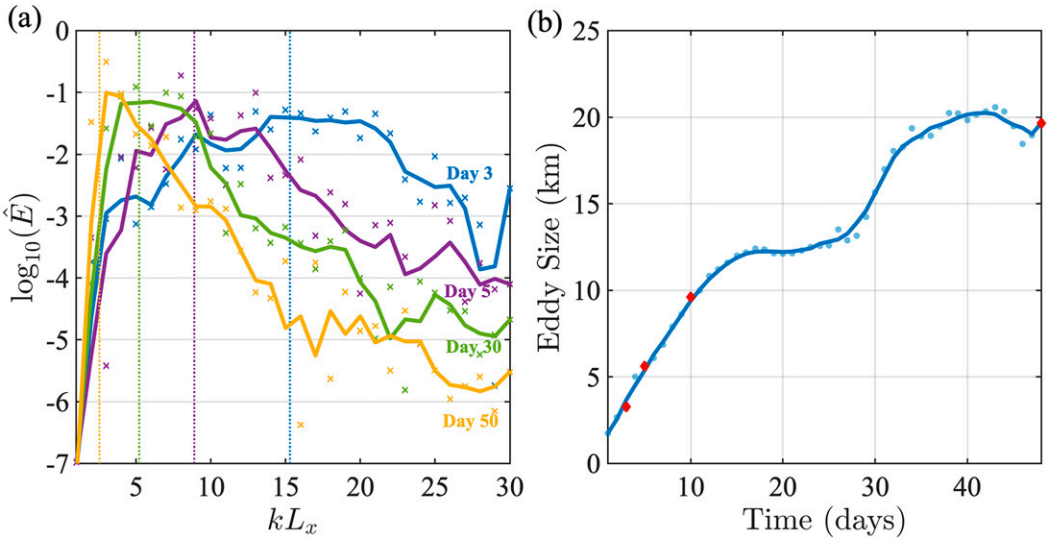

FIG. 8. Diagnosis and evolution of the dominant eddy length scale in our simulations. (a) The normalized kinetic energy spectrum $\hat{E}(k)$ as a function of the spectral wavenumber k. Dotted vertical lines indicate the centroid wavenumber of each spectral curve. Curves are smoothed using the average in y and over a 3-day window. (b) Eddy size D, defined using the centroid wavenumber in Eq. (13), as a function of time in our reference simulation.

following $y \sim (\kappa t)^{1/2}$ (LaCasce 2008). This scaling, which we derive from the analytical solution of the one-dimensional diffusion equation, has previously been applied to quantify effective diffusivities from ocean tracer observations (e.g., LaCasce et al. 2014). However, in our model, buoyancy is continually lost through the surface of the lead, so this simple scaling for κ does not apply. We therefore explicitly solve a one-dimensional forced diffusion equation and optimize the solution to determine the value of κ_ℓ that maximizes agreement with the buoyancy anomalies derived from our 3D simulations.

Our solution procedure is as follows. We solve Eqs. (6) and (7) prognostically for $\langle \overline{b}^x \rangle(y, t)$, , setting $\kappa = \kappa_\ell$ to be a constant. We simplify the surface buoyancy flux by neglecting the surface restoring of potential temperature to the freezing temperature such that

$$\overline{\dot{B}}^x = \begin{cases} -g\beta\dot{\Sigma}(t)/\rho_{\text{ref}}, & |y| < W/2, \\ 0, & |y| > W/2, \end{cases} \tag{9}$$

where $\beta = 8 \times 10^{-4}\ \text{kg g}^{-1}$ is the haline contraction coefficient and $\dot{\Sigma}$ is the surface salt flux in the lead (see Fig. 2c). We discretize the resulting equations using centered finite differences in y, with a grid spacing that matches our 3D simulations, and forward Euler time stepping, ensuring that the time step satisfies the Courant–Friedrichs–Lewy criterion for the Laplacian diffusion equation. We then repeatedly solve this system numerically for $\langle \overline{b}^x \rangle(y, t)$ with varying κ_ℓ. We define the optimal κ_ℓ as that which yields the smallest least-squared difference in $\langle \overline{b}^x \rangle(y, t)$ between the 1D solution and the 3D simulation, over all points in space and time. In Fig. 7c, we plot $\langle \overline{b}^x \rangle(y, t)$ derived from our 1D model using parameters for our 3D reference simulation. In this case, the optimal eddy diffusivity is $\kappa_\ell = 29.1\ \text{m}^2\,\text{s}^{-1}$, which produces a small relative root-mean-square error of 0.6% between the 3D and 1D $\langle \overline{b}^x \rangle(y, t)$ fields. The close resemblance between Figs. 7a and 7c shows that the 1D model produces an accurate estimate of κ_ℓ.

3) EDDY SIZE

We now quantify the dominant size of the eddies formed in our simulations. SCV sizes can be determined by using eddy tracking methods (Tarshish et al. 2018; Wang et al. 2016). However, the geometric simplicity of our model domain allows us to make a more straightforward estimate of the dominant eddy scale using a Fourier mode decomposition. Specifically, we define the velocity anomalies relative to an along-lead average as $u^\dagger = u - \overline{u}^x$ and $v^\dagger = v - \overline{v}^x$ and decompose them as

$$u^\dagger = \int \hat{u}(k) e^{ikx}\, dk \quad \text{and} \tag{10a}$$

$$v^\dagger = \int \hat{v}(k) e^{ikx}\, dk. \tag{10b}$$

Here, k is the wavenumber, and $\hat{u}(k)$ and $\hat{v}(k)$ are the Fourier components of $u^\dagger$ and $v^\dagger$, respectively.

We quantify the dominant eddy size by examining the distribution of EKE (per unit wavenumber) in Fourier space, which is expressed as

$$\hat{E}(k) = \frac{1}{2}\left[|\hat{u}(k)|^2 + |\hat{v}(k)|^2\right]. \tag{11}$$

In Fig. 8a, we plot the spectrum $\hat{E}(k)$ on days 3, 5, 30, and 50 to visualize the evolution of the energy in wavenumber space. For each plotted day we first averaged the Fourier components $\hat{u}(k)$ and $\hat{v}(k)$ in the cross-lead (y) direction, and over a 3-day window. This plot shows that, over time, EKE shifts from

TABLE 2. List of model experiments. Boldface values indicate parameters that deviate from their reference values. For parameter definitions, refer to Table 1.

Batch	Expt	W (km)	H_0 (m)	H_{pyc} (m)	θ_{max} (°C)	S_{max} (psu)	T_{atm} (°C)	r_b ($\times 10^4$ m s^{-1})
Ref	Ref	3	30	150	0.5	34.6	−25	2.5
W	W1	**1**	30	150	0.5	34.6	−25	2.5
	W5	**5**	30	150	0.5	34.6	−25	2.5
	W7	**7**	30	150	0.5	34.6	−25	2.5
	W10	**10**	30	150	0.5	34.6	−25	2.5
H_0	$H_0$10	3	**10**	150	0.5	34.6	−25	2.5
	$H_0$50	3	**50**	150	0.5	34.6	−25	2.5
	$H_0$100	3	**100**	150	0.5	34.6	−25	2.5
	$H_0$200	3	**200**	150	0.5	34.6	−25	2.5
H_{pyc}	H_{pyc}50	3	30	**50**	0.5	34.6	−25	2.5
	H_{pyc}100	3	30	**100**	0.5	34.6	−25	2.5
	H_{pyc}200	3	30	**200**	0.5	34.6	−25	2.5
	H_{pyc}400	3	30	**400**	0.5	34.6	−25	2.5
$\Delta\theta$	θ_{max}0	3	30	150	**0**	34.6	−25	2.5
	θ_{max}0.25	3	30	150	**0.25**	34.6	−25	2.5
	θ_{max}0.75	3	30	150	**0.75**	34.6	−25	2.5
	θ_{max}1	3	30	150	**1**	34.6	−25	2.5
ΔS	S_{max}34.5	3	30	150	0.5	**34.5**	−25	2.5
	S_{max}34.7	3	30	150	0.5	**34.7**	−25	2.5
	S_{max}34.9	3	30	150	0.5	**34.9**	−25	2.5
	S_{max}35	3	30	150	0.5	**35.0**	−25	2.5
T_{atm}	T_{atm}10	3	30	150	0.5	34.6	**−10**	2.5
	T_{atm}20	3	30	150	0.5	34.6	**−20**	2.5
	T_{atm}30	3	30	150	0.5	34.6	**−30**	2.5
	T_{atm}40	3	30	150	0.5	34.6	**−40**	2.5
r_b	$(r_b)_{min}$	3	30	150	0.5	34.6	−25	**0.5**
	$(r_b)_{1.25}$	3	30	150	0.5	34.6	−25	**1.25**
	$(r_b)_5$	3	30	150	0.5	34.6	−25	**5**
	$(r_b)_{max}$	3	30	150	0.5	34.6	−25	**12.5**

relatively small scales at day 3, with energy concentrated between wavelengths of 2.5–3.5 km, to much larger scales at day 50, with energy concentrated around wavelengths of 15–25 km. This suggests that an inverse cascade of energy is taking place, as expected of quasi-two-dimensional turbulence (e.g., Vallis 2006).

To quantify the evolution of the dominant energy-containing length scale more precisely, we define the centroid wavenumber,

$$k_c = \frac{\int k\hat{E}(k)\,dk}{\int \hat{E}(k)\,dk}. \tag{12}$$

The vertical dotted lines in Fig. 8a indicate k_c at days 3, 5, 30, and 50. We then define the eddy diameter D as

$$D = 2\pi/k_c. \tag{13}$$

In Fig. 8b we plot D as a function of time throughout our reference simulation. Consistent with our qualitative inference from the energy spectra, the eddies grow nearly linearly from approximately 1.5 km in size at the start of the simulation until $t \approx$ 15 days. Subsequently, the eddies continue to grow, but with increased temporal variability, and ultimately reach a scale of ~20 km by $t = 50$ days. This suggests that eddy–eddy interactions facilitate the growth of eddies to a size that compares to SCVs observed in sea ice–covered regions (e.g., Zhao et al. 2014).

4. Parameter sensitivity

In section 3 we identified three key quantities of interest in our simulations: the MLD, the eddy diffusivity κ_ℓ, and the dominant eddy size D. In this section, we quantify the sensitivity of these three key quantities to various model parameters to draw further insights into the dynamics of lead eddy formation. Specifically, we vary the lead width W, the initial mixed layer depth H_0, the pycnocline thickness H_{pyc}, the cross-pycnocline temperature difference $\Delta\theta$, the cross-pycnocline salinity difference ΔS, the atmospheric temperature T_{atm}, and the drag velocity r_b. Most of these parameters were chosen on the basis of their role in setting the strength of the buoyancy forcing and stratification, which were shown to be important to the eddy properties in previous modeling studies (Matsumura and Hasumi 2008; Smith et al. 2002).

The sensitivity experiments and their corresponding parameter values are listed in Table 2. The parameter ranges chosen are intended to span a wide range of conditions in the ocean's sea ice covered regions but are perturbed about a reference state that approximates conditions in the southern Weddell Sea (see section 2). The lead width is varied between 1 and 10 km. These lead widths fall within the range that is

observed in nature (Key et al. 1993; Lindsay and Rothrock 1995; Reiser et al. 2020) and that can be represented in our model configuration; smaller widths would necessitate higher resolutions, while larger widths would require larger domains. We explore seasonal and regional values of H_0, ranging from depths as shallow as 10 m, as might occur in the summer, to 200 m, as observed in winters or closer to the shore (Pellichero et al. 2017). Similarly, we examine cases for both shallow and deep pycnoclines, ranging from 50 to 400 m. Vertical temperature and salinity gradients are selected based on observations around Kapp Norvegia (Hattermann 2018). The atmospheric temperature T_{atm} perturbations are selected using typical Antarctic atmospheric temperatures, ranging from −10°C in the summer to −40°C in the winter (Chapman and Walsh 2007). Last, we vary the sea ice drag velocity by over an order of magnitude, ranging from 5×10^{-5} and 1.25×10^{-3} m s^{-1}.

To provide a qualitative sense of the sensitivity of the eddy properties to these parameters, in Fig. 9 we illustrate changes in the model simulations for some of our sensitivity experiments. Specifically, we select cases with $H_{pyc} = 50$ m, $H_0 = 200$ m, $T_{atm} = -40$°C, and $W = 10$ km because these values exhibit some of the most extreme differences from our reference simulation. This figure highlights that changing the initial stratification, the rate of sea ice growth in the lead, and the width of the lead can all qualitatively change the vertical penetration and horizontal spread of buoyancy anomalies, and the character of the resulting eddy field. The sensitivities of the MLD, κ_ℓ, and D are quantified in Figs. 10 and 11 and are discussed in detail below.

a. Mixed layer depth

In Fig. 10, we present the sensitivity of the MLD deepening, ΔMLD = MLD − H_0, across all of our sensitivity experiments. The figure indicates that ΔMLD is most sensitive to the parameters governing the ambient ocean stratification (H_{pyc}, H_0, and ΔS), and to the width of the lead W. Our H_{pyc} sensitivity experiments produce the largest absolute variation in ΔMLD, ranging approximately from 25 to 100 m. Figure 10 also shows that ΔMLD decreases from 75 to 30 m as we increase ΔS. The effects of both H_{pyc} and ΔS can be explained via their relationship with stratification: a weaker stratification allows the plume to penetrate deeper into the pycnocline and thereby deepen the mixed layer depth. Note that, as is the case with lead-driven convection, density is primarily influenced by salinity, and therefore, unlike ΔS, our selected range of $\Delta\theta$ very weakly influences the stratification and thus has a negligible effect on ΔMLD (Fig. 10d).

As we increase the initial mixed layer thickness H_0 from 10 to 200 m, ΔMLD decreases from ~75 to 15 m. Qualitatively, this occurs because for a fixed input of buoyancy, a deeper mixed layer leads to a weaker buoyancy anomaly, when vertically averaged over the mixed layer. Thus, a deeper mixed layer suppresses the penetration of the convection into the pycnocline. As we increase W from 1 to 10 km, ΔMLD increases from 45 to 85 m. The explanation for this sensitivity must necessarily go beyond one-dimensional (vertical) consideration of the mixed layer and pycnocline stratification, suggesting that varying W changes the eddy formation process and the arrest of the mixed layer deepening. This is discussed further in section 5a.

Surprisingly, Fig. 10 shows that varying T_{atm}, and thus the surface buoyancy loss, only weakly influences ΔMLD. This is discussed further in section 5, where we show that this weak sensitivity is consistent with the theoretical prediction of the MLD based on mixed layer buoyancy budget. The influence of sea ice drag is even weaker, and is negligible in comparison with the other parameters, suggesting that the mechanical interaction of lead eddies with the overlying sea ice does not affect their arrest of the mixed layer deepening.

b. Eddy diffusivity

In Fig. 10, we also plot the variations of the bulk eddy diffusivity κ_ℓ, as diagnosed by our 1D model (section 3b), across our sensitivity experiments. These plots indicate that κ_ℓ is most strongly influenced by lead width, and secondarily by H_0 and ΔS.

Our lead width sensitivity experiments produce the largest variations found in κ_ℓ, with values ranging from $\kappa_\ell = 10$ m^2 s^{-1} for a small lead width of $W = 1$ km, to $\kappa_\ell = 50$ m^2 s^{-1} for a large lead width of $W = 10$ km. Figure 9 shows that for $W = 10$ km the buoyancy anomalies spread much more rapidly than in our reference case and are larger in magnitude, while the eddies are more intense and more numerous. Taken together, these suggest that the larger net buoyancy loss in wide leads produces a more intense eddy field that spreads buoyancy anomalies more efficiently and suggests that the largest leads should play an outsized role in modifying the upper-ocean stratification under sea ice.

The eddy diffusivity κ_ℓ exhibits differing responses to the stratification parameters: over the ranges of H_0 and ΔS explored in our sensitivity experiments, κ_ℓ increases from ~25 to ~45 m^2 s^{-1}. However, κ_ℓ varies by less than a factor of 2 in response to an eightfold variation in H_{pyc}. These responses are less amenable to interpretation than the response of the MLD to the stratification parameters, but we will provide further insight into these sensitivities via our scaling for κ_ℓ in section 5b. Once again, as the stratification weakly varies with potential temperature, $\Delta\theta$ has little influence on κ_ℓ over the range considered here.

Other parameters that exert relatively weaker influences on κ_ℓ are T_{atm} and r_b. Here, κ_ℓ increases between 20 and 30 m^2 s^{-1} for an increasing T_{atm}, with little sensitivity below $T_{atm} = -25$°C. In section 5b we show that this is because κ_ℓ is related to the square root of the EKE, which in turn is linearly related to the surface buoyancy loss, and thus T_{atm}. Surprisingly, increasing the sea ice drag has very little impact on the eddy field and its effect on spreading buoyancy anomalies via κ_ℓ. This suggests that the lead eddy SCVs are largely shielded from direct mechanical interaction with the mixed layer, despite forming at the top of the pycnocline.

c. Eddy size

Figure 9 (right column) suggests that although there are substantial differences in the cross-lead migration of eddies between simulations, the sizes of the eddies are visually similar. Consistent with this observation, we find that there is relatively

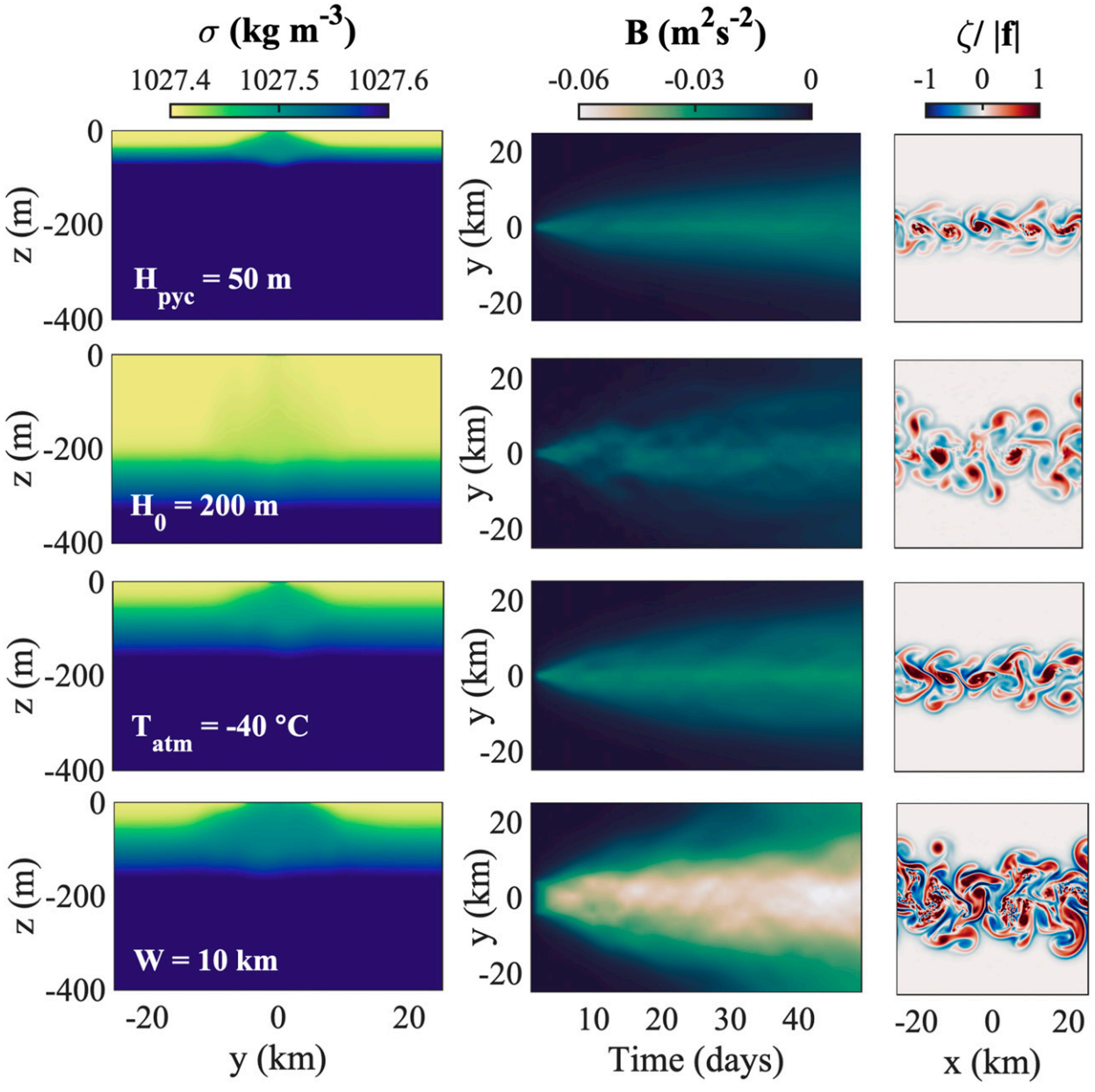

FIG. 9. Illustration of the model sensitivity to key control parameters: (top) $H_{pyc} = 50$ m, (top middle) $H_0 = 200$ m, (bottom middle) $T_{atm} = 40$°C, and (bottom) $W = 10$ km for (left) the along-lead-averaged potential density field at day 10 of the simulation, (center) the depth-integrated and along-lead-averaged buoyancy field as a function of cross-lead distance and time, and (right) the relative vorticity normalized by the Coriolis parameter, plotted at day 10 at the diagnosed MLD at day 10 (see section 3a). See Figs. 4, 5d, and 7c for comparisons with the reference case.

little spread in the eddy size D early in the simulations ($t \leq 10$ days), as shown in Fig. 11. Later in the simulations the eddy size exhibits substantial intra- and intersimulation variability that largely precludes any firm relationships being drawn between D and our sensitivity parameters.

Two notable exceptions are the sensitivity experiments with extreme values of W and T_{atm}, which are labeled in Fig. 11. In these experiments D typically lies around two standard deviations from the mean, suggesting that there is a distinguishable increase in D with both W and T_{atm}. A speculative interpretation is that stronger net buoyancy loss within the lead produces a more energetic eddy field, which favors more frequent eddy–eddy interactions and thus a more rapid ascent in the dominant energy-containing length scales of the eddies. However Figs. 9 and 11 show that even in these extreme sensitivity experiments, D exhibits relatively modest departures (±40%) from the reference case, and in general the strongest predictor of the eddy size is the time since the opening of the lead.

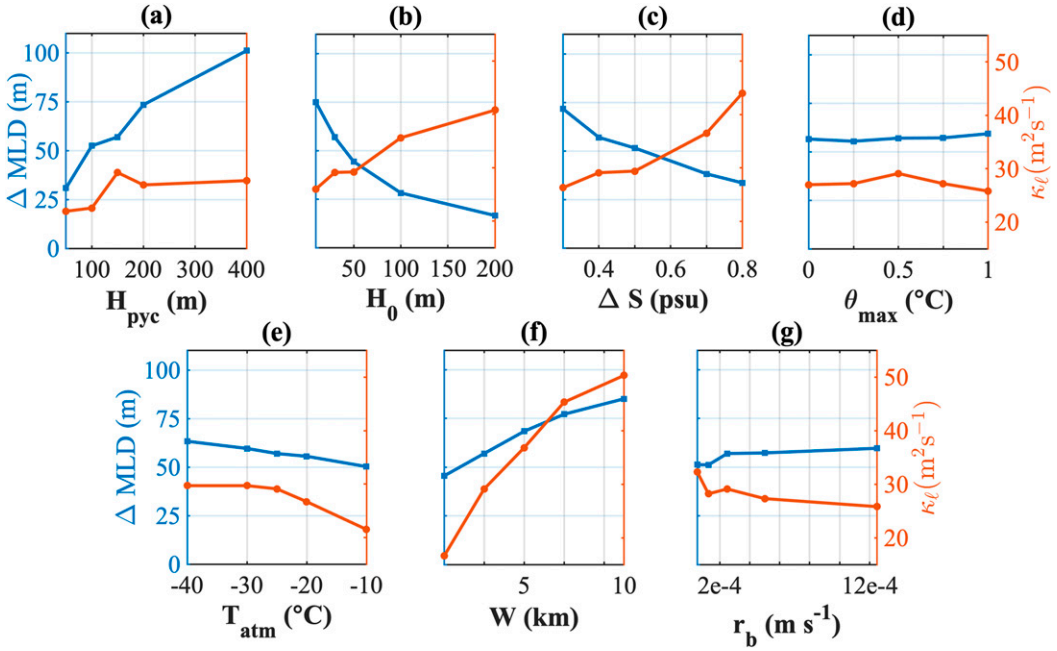

FIG. 10. Dependence of the mixed layer deepening ΔMLD = MLD − H_0 (left axis) and bulk buoyancy diffusivity κ_ℓ (right axis) to various model configuration parameters. We plot sensitivities to (a) pycnocline thickness $H_{\rm pyc}$, (b) atmospheric temperature $T_{\rm atm}$, (c) initial mixed layer depth H_0, (d) lead width W, (e) pycnocline temperature gradient $\Delta\theta$, (f) pycnocline salinity gradient ΔS, and (g) surface drag coefficient r_b.

5. Scaling for under-lead eddy dynamics

To provide further insight into the dynamics of lead eddies, we now pose scalings that relate the MLD, κ_ℓ, and D to the properties of the lead and the ambient ocean stratification. Note that the scalings developed in this section are not intended as parameterizations but rather are intended to confer fundamental understanding of the processes occurring beneath leads.

a. *Mixed layer depth*

To predict the MLD, we first pose a simplified model for the evolution of the MLD in the absence of any lead eddy formation and lateral spreading of buoyancy anomalies. We then show that truncating the model after a few days, around the time that lead eddies are generated, yields an accurate prediction of the long-term MLD in our simulations.

We solve for the MLD, which we denote as H_m, at each time t in our simulations. To determine H_m, we idealize the stratification as a well-mixed layer for $z > -H_m$ and assume that it is identical to the model's initial stratification [defined in Eqs. (1a) and (1b)] for $z < -H_m$. More precisely, we assume θ and S profiles of the form

$$\theta = \begin{cases} \theta_f, & z > -H_m, \\ \theta_0(z), & z < -H_m, \end{cases} \quad \text{and} \tag{14a}$$

$$S = \begin{cases} S^\star, & z > -H_m, \\ S_0(z), & z < -H_m. \end{cases} \tag{14b}$$

Here the potential temperature of the mixed layer is assumed to be fixed at the surface freezing temperature, θ_f, while the salinity of the mixed layer is an unknown $S^\star$. We can relate $S^\star$ to H_m by assuming that total salinity is conserved above $z = -H_m$,

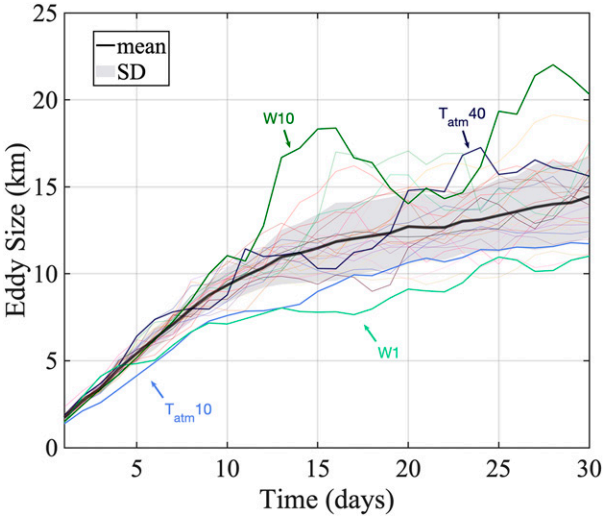

FIG. 11. Evolution of the dominant eddy length scale. We plot the eddy size, as diagnosed from the kinetic energy spectrum (see section 3), as a function of time for all of our 3D model simulations. The black line shows the mean, and the shaded area indicates 1 standard deviation about the mean at each point in time. Time series of the W (green shades) and $T_{\rm atm}$ (blue shades) experiments are labeled.

$$S^{\star} = \frac{1}{H_m}\left[\int_{-H_m}^{0} S_0(z)\,dz + \frac{\Sigma}{\rho_0}\right], \tag{15}$$

where Σ is again the time-integrated downward surface salt flux in grams per meter squared. These profiles are illustrated for the simple case of piecewise-linear initial $S_0(z)$ and $\theta_0(z)$, profiles in Fig. 12. Note that both $\theta(z)$ and $S(z)$ are discontinuous across the base of the mixed layer.

To determine H_m, we assume that the surface buoyancy loss deepens the mixed layer until the stratification at the base of the mixed layer becomes statically stable. The threshold for static stability is crossed when the in situ density difference between the base of the mixed layer and the top of the pycnocline is equal to zero,

$$\rho(S^{\star}, \theta_f, -H_m) = \rho[S_0(-H_m), \theta_0(-H_m), -H_m]. \tag{16}$$

Nonlinearities of the equation of state may play an important role in convective processes at high latitudes (Akitomo 2005). We therefore determine the in situ density using a simplified nonlinear equation of state that permits both thermobaric and cabbeling effects, similar to that given by Vallis (2006):

$$\rho(S,\theta,z) = \rho_0\Big\{1 + \beta(S - S_{\mathrm{ref}}) + \gamma(z - z_{\mathrm{ref}}) - [\alpha_0 + \alpha_z(z - z_{\mathrm{ref}})](\theta - \theta_{\mathrm{ref}}) - \frac{1}{2}\alpha_\theta(\theta - \theta_{\mathrm{ref}})^2\Big\}. \tag{17}$$

Here, α is the thermal expansion coefficient (K^{-1}), β is the haline contraction coefficient (psu^{-1}), and γ is the Boussinesq compressibility coefficient (m^{-1}). The thermal expansion coefficient is allowed to depend on z and θ to capture the leading nonlinearities due to thermobaricity and cabbeling, respectively:

$$\alpha = -\rho_0^{-1}\partial_\theta \rho = \alpha_0 + \alpha_z(z - z_{\mathrm{ref}}) + \alpha_\theta(\theta - \theta_{\mathrm{ref}}). \tag{18}$$

Here α_0, α_θ, and α_z are the reference thermal expansion coefficient (K^{-1}), the cabbeling parameter (K^{-2}), and the thermobaricity parameter ($\mathrm{K}^{-1}\,\mathrm{m}^{-1}$), respectively. The "ref" subscripts denote reference values about which the full equation of state has been Taylor-expanded to produce Eq. (17). For each experiment we select $S_{\mathrm{ref}} = S_{\min}$, $\theta_{\mathrm{ref}} = \theta_f$, and $Z_{\mathrm{ref}} = -H_0$. We then calculate the coefficients α_0, β, α_θ, and α_z using the Gibbs Seawater Oceanographic Toolbox (McDougall and Barker 2011). The values of these coefficients for the reference case are $\alpha_0 = 2.56 \times 10^{-5}\,\mathrm{K}^{-1}$, $\beta = 7.87 \times 10^{-4}\,\mathrm{psu}^{-1}$, $\alpha_\theta = 1.41 \times 10^{-5}\,\mathrm{K}^{-2}$, and $\alpha_z = 3.20 \times 10^{-8}\,\mathrm{K}^{-1}\,\mathrm{m}^{-1}$.

Substituting Eqs. (14a), (14b), (15), and (17) into Eq. (16) yields a single nonlinear equation that solves for the mixed layer depth H_m. In appendix A, we discuss the specific case of a piecewise-linear stratification, which is shown in Fig. 12. This results in a cubic equation for H_m, which can be solved to obtain H_m as a function of H_0, H_{pyc}, $S_{\min}$, θ_f, $S_{\max}$, $\theta_{\max}$, Σ and θ_{ref}. In Fig. 6b, we plot the predicted H_m as a function of time for our reference case. As our simplified model is one-dimensional, it predicts that the MLD deepens continuously within the lead, whereas in 3D simulations, baroclinic instability halts MLD deepening despite sustained surface buoyancy loss. The 1D model compares favorably to our 2D simulations for the first 10–15 days, but then overpredicts the MLD at later times. This is consistent with the modest horizontal spreading of buoyancy anomalies in the 2D simulations shown in Fig. 4, which is not accounted for in our simplified model.

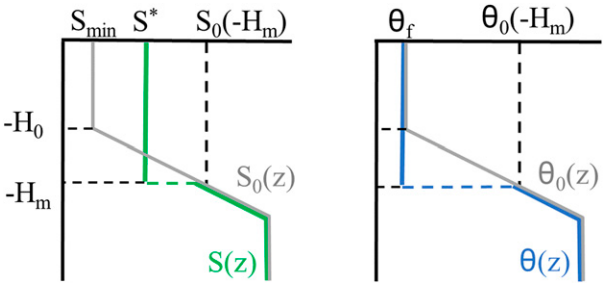

FIG. 12. Illustrations of idealized piecewise linear stratification for (left) salinity S and (right) potential temperature θ used in our theory (section 5a); $S_0(z)$ and $\theta_0(z)$ are the stratifications at $t = 0$ (gray line), and $S(z)$ and $\theta(z)$ are the profiles after lead-induced convection has penetrated into the pycnocline (colored lines).

In our simulations, MLD deepening ceases around days 2–4, around the time that nonlinear eddies begin to emerge (see Fig. 5). This time scale may be compared with the time scale for exponential growth of unstable baroclinic waves (Eady 1949), $\tau_{\mathrm{Eady}} = \mathrm{Ri}^{1/2}/|f|$. Approximating the Richardson number Ri using the baroclinic shear in the mixed layer and the vertical stratification of the pycnocline, we obtain

$$\mathrm{Ri} = \frac{N^2}{V_z^2} \approx \frac{f^2 \overline{b}_z|_{\mathrm{pyc}}}{(\overline{b}_y|_{\mathrm{ML}})^2} \sim \frac{f^2 \dfrac{g(\alpha\Delta\theta - \beta\Delta S)}{H_{\mathrm{pyc}}}}{\left[\dfrac{g\beta(S^{\star} - S_{\min})}{\frac{1}{2}W}\right]^2}. \tag{19}$$

For typical values of $S^{\star}$ after one day of ML deepening, we obtain $\tau_{\mathrm{Eady}} \approx 0.3$ days. Thus, the arrest of the ML deepening occurring several Eady growth time scales later is qualitatively consistent with linear baroclinic instability of the lead convection zone.

Attempting to predict the time at which nonlinear eddies emerge from Eq. (19) is challenging because $S^{\star}$ varies sharply over the first few days of the lead evolution. Therefore, we instead simply assume that the ML deepening is consistently arrested around days 2–4 as nonlinear eddies start to form and spread buoyancy anomalies laterally. In Fig. 13a, we compare the predicted H_m, averaged between days 2 and 4, with the simulated mixed layer depth in the corresponding 3D simulations, averaged over days 10–50. The predicted and diagnosed MLDs agree closely, with a correlation of $r \approx 0.95$.

The most significant shortcoming of our simplified model is that it fails to capture the simulated deepening of the ML with increasing lead width W. This shortcoming may be mitigated using Eq. (19), which suggests that $\mathrm{Ri} \sim W^2$, and thus that $\tau_{\mathrm{Eady}} \sim W$; that is, for wider leads the ML should deepen for longer before it is arrested by eddy formation.

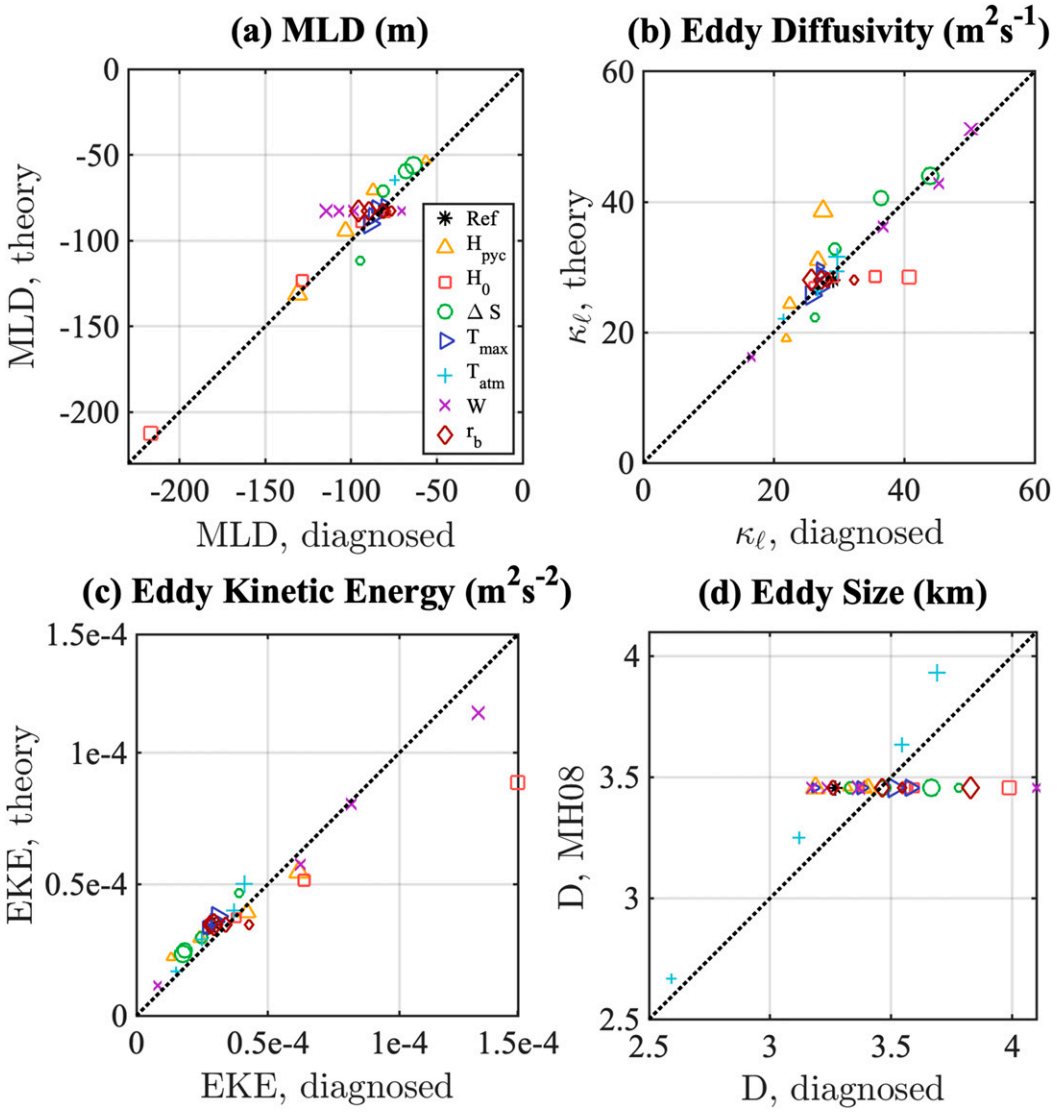

FIG. 13. Evaluations of our scaling-based predictions of key mixed layer and eddy properties against our 3D simulations. (a) Diagnosed MLD, averaged over days 10—50, vs the theoretically predicted MLD, averaged over days 2–4 (see section 5b). (b) Diagnosed bulk buoyancy diffusivity κ_ℓ (see section 3b) vs the prediction given by Eq. (23). (c) Diagnosed eddy kinetic energy, averaged over the entire volume and duration of the simulation, vs the theoretical upper bound for the EKE at the end of the simulation. The latter is calculated as $\mathrm{EKE_{ML}}H_m/H$ where $\mathrm{EKE_{ML}}$ is given by Eq. (21). (d) Eddy size D at $t = 3$ days vs the scaling prediction of Matsumura and Hasumi (2008). In each panel different symbol shapes correspond to different parameter variation experiments (see legend), with larger shapes indicating larger absolute values of the corresponding parameter.

b. *Eddy diffusivity*

We now propose a scaling for κ_ℓ to quantify the horizontal buoyancy spread due to eddies. Our scaling is based on mixing-length theory (Prandtl 1925),

$$\kappa_\ell \sim U_e \ell, \tag{20}$$

where U_e is an eddy velocity scale and ℓ is a mixing length. This formulation serves as the basis of various proposed parameterizations of ocean mesoscale eddies (e.g., Visbeck et al. 1997; Jansen et al. 2015; Wang and Stewart 2020). We anticipate U_e being related to EKE via the relationship $U_e \sim \mathrm{EKE}^{1/2}$. The kinetic energy within the system is all ultimately sourced from the buoyancy loss in the lead, which creates available potential energy (APE, e.g., Winters et al. 1995). Baroclinic instability converts this APE into kinetic energy and sustains the eddy field (Smith et al. 2002; Matsumura and Hasumi 2008).

To develop a scaling for κ_ℓ, in appendix B we use the energy budget to derive an upper bound on the EKE in the mixed layer, $\mathrm{EKE_{ML}}$. The upper bound is obtained by assuming

(i) that nonconservative terms in the energy budget are negligible, (ii) assuming that all buoyancy anomalies injected at the surface are carried to the base of the mixed layer, (iii) that the energy flux downward across the mixed layer base is zero, and (iv) that the mean kinetic energy and the vertical EKE are negligible relative to the horizontal EKE, i.e., KE ≈ EKE. This yields the following bound for the horizontally and vertically averaged EKE in the ML:

$$\mathrm{EKE}_{\mathrm{ML}} = \frac{1}{H_m L_x L_y}\int_{-H_m}^{0} dz \iint_A \mathrm{EKE}\, dA \lesssim \frac{BW}{L_y}. \tag{21}$$

Here, H_m is the theoretically predicted mixed layer depth averaged over days 2–4 (see section 5a), and $B = \int_0^{t_0} \dot{B}\, dt$ is the time-integrated upward surface buoyancy flux.

Figure 13b shows that the EKE diagnosed from our simulations compares very well ($r \approx 0.95$) to the EKE predicted by Eq. (21). The coefficient of proportionality is $C_{\mathrm{EKE}} \approx 0.02$, suggesting that the EKE scales closely with Eq. (21), but that in practice the actual EKE is only a few percent of the theoretical upper bound. Given the weak dependence on surface drag (Fig. 10), this is likely due to energy dissipation in the convective zone beneath the lead.

Conventional scalings of baroclinic eddy fluxes expect the mixing-length scale to vary with drag (Thompson and Young 2006; Larichev and Held 1995). However, since lead eddies appear to be independent of drag, we set the mixing-length scale to be the first Rossby radius of deformation imposed by the ambient stratification; that is, $\ell = R_d$, where

$$R_d = \frac{1}{\pi f_0}\int_{-H}^{0} N\, dz \tag{22}$$

and N is the buoyancy frequency. Thus, Eq. (20) suggests that the mixed layer–averaged κ_ℓ scales as

$$\kappa_\ell \sim \mathrm{EKE}_{\mathrm{ML}}^{1/2} R_d \sim C_\kappa \left(\frac{W}{L_y} B\right)^{1/2} R_d \tag{23}$$

where $\mathrm{EKE}_{\mathrm{ML}}$ is given in Eq. (21) and $C_\kappa = 0.17$ is the eddy diffusivity scaling coefficient. In Fig. 13c we compare these results with κ_ℓ diagnosed from our 3D simulations, using our 1D model (section 3b), finding a Pearson correlation of $r \approx 0.86$. The largest errors in this scaling result from our experiments with varying pycnocline thickness H_{pyc} and initial mixed layer depth H_0.

c. Eddy size

A scaling for the eddy size has previously been proposed by Matsumura and Hasumi (2008), so here we test their scaling against our simulations. Matsumura and Hasumi (2008) suggest two scaling regimes for the lead eddy deformation radius R_ℓ, depending on its size relative to the lead width W. In all of our simulations, $R_\ell \leq W$, so we adopt the scaling

$$R_\ell \sim \sqrt{B(t)}/f, \tag{24}$$

where f is the Coriolis parameter and $B(t)$ is the time-integrated surface buoyancy flux per unit area.

In Fig. 13d, we compare the eddy size predicted by Eq. (24) with our model results at $t = 3$ days. We chose this time because it occurs earlier than the pronounced divergence in the diagnosed eddy sizes in Fig. 11 and yielded the maximum correlation of $r \approx 0.6$, with a coefficient or proportionality of ~1.2. Notice that $t = 3$ days coincides with the time at which the MLD deepening is arrested by eddy generation and is consistent with baroclinic growth over several Eady time scales (see section 5a). This suggests that eddies grow predictably up to $t \sim 3$ days, after which the evolution of the eddy scale becomes dominated by merging events and becomes increasingly chaotic.

In comparison with the correlations found for MLD, κ, and EKE, Fig. 13d yields a relatively low correlation for D. This is in part because our diagnosed D typically only vary by around 10% due to changes in the model parameters (Fig. 10). An exception is that D varies by around 20% in response to changes in the atmospheric temperature T_{atm}, which is captured by the dependence of B on T_{atm} in Eq. (24). This may be indicative of sensitivities due to our algorithm for diagnosing eddy sizes, of chaotic behavior in the eddy size evolution even during the initial phase of growth, or of additional dependencies on the model parameters not captured by the theory of Matsumura and Hasumi (2008).

6. Discussion and conclusions

In this study we developed numerical simulations of (sections 2–4) and scalings to explain (section 5) the dynamics of eddies generated by brine rejection and convection within freezing leads. Brine rejection in leads contributes substantially to surface buoyancy fluxes in sea ice covered regions, while eddies serve to horizontally redistribute these localized buoyancy anomalies (Smith et al. 1990; Morison et al. 1992). Previous studies have performed similar idealized numerical simulations to isolate the dynamics of lead eddies, primarily motivated by Arctic conditions (Smith et al. 2002; Matsumura and Hasumi 2008). Our study advances our understanding of lead eddies by posing the simulations in a parameter regime primarily motivated by Antarctic conditions, while also including regimes relevant to the Arctic. We focus on the vertical and lateral spread of lead-input buoyancy anomalies, which lack quantitative understanding (Nguyen et al. 2009), and on the potential for lead eddies to contribute to the under-sea-ice eddy field in polar regions (Zhao et al. 2014).

In section 3a, we showed that our model produces a qualitatively similar phenomenology of lead eddy formation as has been described in previous studies (Bush and Woods 1999, 2000; Smith et al. 2002; Matsumura and Hasumi 2008). Briefly, brine rejection in the lead results in localized convection that deepens the surface mixed layer (see Fig. 4). After 2–4 days, the convective filament becomes baroclinically unstable (see Fig. 5), resulting in the formation of eddies and the arrest of the mixed layer deepening. The eddies then merge, grow, and drift in the cross-lead direction, spreading buoyancy anomalies laterally as they do so (see Fig. 7). We identified three key properties that characterize this eddy formation process, and developed methods to quantify them: the mixed layer depth,

the bulk eddy diffusivity κ_ℓ, and the eddy size D. The MLD and κ_ℓ directly quantify the vertical and horizontal spreading of buoyancy anomalies, respectively, while D allows us to assess the potential for lead eddies to contribute to the under-sea-ice eddy field.

In section 4, we performed a series of sensitivity experiments to determine which properties of the ambient ocean stratification and the buoyancy loss through the lead most strongly influence the MLD, κ_ℓ, and D. To complement these experiments, in section 5 we developed scalings relating the MLD, κ_ℓ, and D to the parameters of the lead and the ambient ocean stratification. A synthesis of the key insights from the experiments and scalings is as follows:

- We found that the evolution of the MLD is closely predicted by a mixed layer buoyancy budget (Fig. 13), truncated after 2–4 days to account for the arrest of the mixed layer deepening by eddy formation (section 5a). This time scale is qualitatively consistent with baroclinic growth over an exponential Eady (1949) time scale. Consequently, the MLD is most sensitive to parameters controlling the initial stratification (Fig. 10). However, our scaling does not capture the sensitivity of the MLD to the lead width W (Fig. 13); in section 5a, we speculate wider leads may reduce the horizontal buoyancy gradients, increasing the bulk Richardson number and thus the Eady growth time scale.
- The bulk eddy diffusivity κ_ℓ is closely predicted by a mixing-length-theory-based scaling (Prandtl 1925), with the eddy velocity determined by the eddy kinetic energy and the length scale determined by the Rossby radius of deformation R_d imposed by the ambient stratification. The EKE, in turn, scales with the total potential energy input associated with the buoyancy loss within the lead (Figs. 13b,c). As a result, κ_ℓ is sensitive to parameters controlling the ambient ocean stratification, which set R_d, and κ_ℓ also varies with the total buoyancy loss in the lead, which is determined by the atmospheric temperature and the lead width (Fig. 10).
- In all of our simulations, D grows nearly linearly at a rate of $0.7\,\mathrm{km\,day^{-1}}$ until $t \sim 10$ days, after which the flow becomes chaotic and the eddies grow to a scale of ~15 km (Fig. 11). Thus, the late-time ($t \geq 10$ days) D is only weakly related to the lead buoyancy loss and the ambient stratification and is most closely predicted by time since the lead opened. Early in the evolution, the sizes of the eddies are more predictable, showing a modest correlation with the eddy size scaling proposed by Matsumura and Hasumi (2008) at $t \cong 3$ days, corresponding to several Eady growth time scales. However, the eddy sizes at this time vary little, typically ranging from 2.5 to 4 km, and are very weakly related to the evolution of D at later times. The longevity of the lead eddies and their comparable size to observed SCVs under sea ice (Zhao et al. 2014) suggests that they may contribute to the under-sea-ice eddy field in polar regions.

Across all three of the properties described above, we consistently found that the ocean–sea ice drag velocity r_b had a very weak influence. One might expect that mechanical stresses between the ocean and sea ice would draw energy from the eddy field, reducing κ_ℓ and D and potentially increasing the MLD. The insensitivity to r_b reported here suggests that the vertical structure of eddies shields them from significant mechanical interaction with the sea ice. This is consistent with Meneghello et al. (2021), where it was found that subsurface eddies are shielded from friction at the surface in a parameter regime representative of Arctic leads. In addition, it is also conceivable that this result could change with a more comprehensive representation of the ice–ocean boundary layer and ice–ocean stresses (cf. Cole et al. 2014; McPhee 2012; Park and Stewart 2016).

These results expand our understanding of under-lead eddy features and the role of leads in upper-ocean dynamics in ice covered regions. However, our idealized modeling approach caries a number of caveats that limit the generalizability of our findings. In particular, we exclude thermodynamics and dynamics of the sea ice, and coupling between the atmosphere and ocean. Previous studies (Kantha 1995; Skyllingstad and Denbo 2001; Heorton et al. 2017) have also indicated that introducing sea ice velocities influence the mixing and circulation beneath leads. Incorporating these influences might yield more accurate predictions of the convective plume depth and the spreading of buoyancy anomalies due to eddies, and it would be particularly interesting to examine these influences on the size and longevity of lead eddies. Furthermore, we do not include the effects of wind within the lead. Winds can herd the ice downwind of the lead and allow for a gradual advancement upward. This process affects the sea ice growth rate, which allows waters to remain at their freezing temperatures, thereby increasing the surface heat and salt fluxes (Bauer and Martin 1983). Another mechanism that can potentially increase these fluxes is the formation of frazil and grease ice (Kantha 1995; Skyllingstad and Denbo 2001; Wilchinsky et al. 2015; Heorton et al. 2017). These mechanisms are not accounted for in our model and may further increase the surface buoyancy fluxes within the lead.

We also note the large-scale advection for both the mean flow and ice drift within the interior of the Ross/Weddell gyres (typically both reaching a few centimeters per second; e.g., Naveira Garabato et al. 2002; Holland and Kwok 2012) are relatively small in comparison with the lead dynamics, and their effects are therefore not considered in this idealized study. However, these assumptions may make our findings less applicable to strong current systems such as the Antarctic Circumpolar Current or Antarctic Slope Current. Similarly, as the regime studied here examines buoyancy-dominating flows with lead widths greater than 1 km, the stress curl across the lead is considered small relative to the lead event. However, these processes may be important to examine when studying different flow regimes or smaller leads (e.g., Bourgault et al. 2020).

In summary, our findings indicate that lead eddies have the potential to contribute to the eddy field observed in polar haloclines and support scaling relationships of the MLD beneath leads and the horizontal eddy diffusion of density anomalies. These findings provide significant progress toward understanding both the eddy field and the role leads play in upper-ocean dynamics in ice-covered regions and may guide improved parameterizations of the effects of unresolved leads

in general circulation models. Further work is required to assess how well these findings apply to coupled sea ice and ocean model experiments, and to cases in which lead geometries and ice drift patterns are more complex than those considered here. Further work is also required to quantitatively estimate the contribution of eddies to the under-sea-ice eddy field; this will require extensive observations of the eddy field in polar regions, which are particularly lacking around Antarctica.

Acknowledgments. This material is based in part upon work supported by the National Science Foundation under Grants ANT-1543388 and OCE-1751386, and by the National Aeronautics and Space Administration ROSES Physical Oceanography program under Grant 80NSSC19K1192. This work used the Extreme Science and Engineering Discovery Environment (XSEDE, Towns et al. 2014), which is supported by National Science Foundation Grant ACI-1548562. The authors thank Dimitris Menemenlis for providing access to the LLC4320 model simulation output that was used to create Fig. 1. The authors thank two anonymous reviewers for many constructive comments that improved the submitted paper.

APPENDIX A

Theoretical Mixed Layer Depth

In this appendix we derive an explicit analytical prediction for the mixed layer depth, following the theory posed in section 5. To derive this prediction, we approximate the initial salinity and temperature profiles, $S_0(z)$ and $\theta_0(z)$, as piecewise-linear functions of depth:

$$S_0(z) = \begin{cases} S_{\min}, & z_0 \le z \le 0 \\ \dfrac{S_{\min}(z - z_{\rm pyc}) - S_{\max}(z - z_0)}{H_{\rm pyc}}, & z_{\rm pyc} \le z \le z_0, \\ S_{\max}, & z \le z_{\rm pyc} \end{cases} \quad \text{and} \tag{A1}$$

$$\theta_0(z) = \begin{cases} \theta_f, & z_0 \le z \le 0 \\ \dfrac{\theta_f(z - z_{\rm pyc}) - \theta_{\max}(z - z_0)}{H_{\rm pyc}}, & z_{\rm pyc} \le z \le z_0. \\ \theta_{\max}, & z \le z_{\rm pyc} \end{cases} \tag{A2}$$

Here $z_0 = -H_0$ corresponds to the base of the mixed layer at $t = 0$ and $z_{\rm pyc} = -(H_{\rm pyc} + H_0)$ corresponds to the base of the pycnocline. These piecewise functions are illustrated in Fig. 12.

We first combine Eqs. (16) and (17) to obtain

$$\beta(S^\star - S_m) - (\alpha + \alpha_z H_m)(\theta_f - \theta_m) - \frac{\alpha_\theta}{2}[(\theta_f - \theta_m)(\theta_f + \theta_m - 2\theta_{\rm ref})] = 0. \tag{A3}$$

Here we define $S_m = S_0(-H_m)$ and $\theta_m = \theta_0(-H_m)$, and from Eq. (15) we have $S^\star = S^\star(H_m)$. Thus Eq. (A3) is an equation with a single unknown, H_m. To solve, we first write S_m and θ_m explicitly in terms of H_m using Eqs. (A1) and (A2):

$$S_m = \frac{S_{\min}(-H_m + H_0 + H_{\rm pyc}) - S_{\max}(-H_m + H_0)}{H_{\rm pyc}} \quad \text{and} \tag{A4}$$

$$\theta_m = \frac{\theta_f(-H_m + H_0 + H_{\rm pyc}) - \theta_{\max}(-H_m + H_0)}{H_{\rm pyc}}. \tag{A5}$$

Next, we evaluate the integral in Eq. (15) using the initial salinity profile given by Eq. (A1) to obtain

$$S^\star = S_{\min} + \frac{\Sigma}{\rho_0 H_m} + \frac{(H_m - H_0)^2(S_{\max} - S_{\min})}{2H_m H_{\rm pyc}}. \tag{A6}$$

Last, we substitute Eqs. (A4)–(A6) into Eq. (A3) to obtain a cubic polynomial equation for H_m,

$$\left(\alpha_z + \frac{\alpha_2}{H_0}\right)H_m^3 + (\alpha_1 - \alpha_z H_0 - 2\alpha_2 - \alpha_3)H_m^2 + H_0(\alpha_2 - \alpha_1)H_m + \frac{\beta\Sigma}{\rho_0}\frac{H_{\rm pyc}}{\theta_{\max} - \theta_f} + \alpha_3 H_0^2 = 0. \tag{A7}$$

Here we define constants $\alpha_1 = \alpha + \alpha_\theta(\theta_f - \theta_{\rm ref})$, $\alpha_2 = \alpha_\theta H_0(\theta_{\max} - \theta_f)/(2H_{\rm pyc})$, and $\alpha_3 = \beta[2(S_{\max} - S_{\min})]/(\theta_{\max} - \theta_f)$. Note that we set $\theta_{\rm ref} = \theta_f$, as discussed in section 5a. Although Eq. (A7) can in principle be solved analytically for H_m, the mathematical form of this solution yields little additional physical insight, so in practice we solve Eq. (A7) numerically.

APPENDIX B

Constraints on Domain-Averaged Eddy Kinetic Energy

In this appendix we use the model energy budget to derive an upper bound on the horizontally averaged eddy kinetic energy. This derivation supports our scalings for the EKE and bulk buoyancy diffusivity in section 5b. We start from the nonhydrostatic Boussinesq momentum equations solved in our simulations,

$$\frac{\partial \mathbf{u}}{\partial t} + (\nabla \times \mathbf{u} + f\hat{\mathbf{z}}) \times \mathbf{u} + \nabla\left(\phi + \frac{1}{2}\mathbf{u}^2\right) = b\hat{\mathbf{z}} + \mathscr{N}, \tag{B1}$$

where $\mathbf{u}$ is the three-dimensional velocity vector, f is the Coriolis parameter, $\phi = p/\rho_0$ is the dynamic pressure, $b = -g(\rho - \rho_0)/\rho_0$ is the buoyancy, and $\mathscr{N}$ denotes nonconservative effects due to surface drag and viscosity. To obtain an evolution equation for the kinetic energy, we take the vector product of Eq. (B1) with $\mathbf{u}$,

$$\frac{\partial}{\partial t}\mathrm{KE} + \nabla \cdot \mathbf{F}_{\rm KE} = wb + \mathscr{N}. \tag{B2}$$

Here $\mathrm{KE} = 0.5\mathbf{u}^2$ is the kinetic energy and $\mathbf{F}_{\rm KE} = \mathbf{u}(0.5\mathbf{u}^2 + \phi)$ is the KE flux. We now consider the kinetic energy budget above an arbitrary vertical level $z = z_0 < 0$. Integrating over the volume $V(z_0)$ enclosed between $z = z_0$ and $z = 0$, we obtain

$$\frac{\partial}{\partial t}\iiint_V \mathrm{KE}\, dV = -\iiint_V \nabla \cdot \mathbf{F}_{\rm KE}\, dV + \iiint_V wb\, dV + \mathscr{N} = \iint_A F^{(z)}_{\rm KE}\big|_{z=z_0}\, dA + \iiint_V wb\, dV + \mathscr{N}, \tag{B3}$$

where A denotes the horizontal area of the plane $z = z_0$ and $F_{\mathrm{KE}}^{(z)}$ is the vertical component of the KE flux. Here we have rewritten the first term on the right-hand side using the divergence theorem, making use of our domain's horizontal periodicity and surface boundary condition of zero surface-normal flow. Finally, to obtain an expression for the kinetic energy we integrate Eq. (B3) from $t = 0$ to an arbitrary time $t = t_0$,

$$\iiint_V \mathrm{KE}\, dV = \int_0^{t_0} dt \iint_A F_{\mathrm{KE}}^{(z)}|_{z=z_0}\, dA + \int_0^{t_0} dt \iiint_V wb\, dV + \mathscr{N}. \tag{B4}$$

Here we have used the initial condition $\mathrm{KE}|_{t=0} = 0$.

The primary source of KE in the model domain is the second term on the right-hand side of Eq. (B3), which quantifies the production of KE from potential energy. We now constrain this term by considering the buoyancy budget in our model domain. An approximate evolution equation for the buoyancy is

$$\frac{\partial b}{\partial t} + \nabla \cdot (\mathbf{u}b) \approx -\frac{\partial F_b}{\partial z}. \tag{B5}$$

Here we have assumed that the buoyancy is materially conserved, which is accurate for a buoyancy variable defined using potential density but omits contributions due to thermobaricity and cabbeling that would arise if the full in situ density were used to define the buoyancy. We define F_b as the upward surface buoyancy flux; that is,

$$F_b = \begin{cases} \dot{B}, & z = 0 \quad \text{and} \quad |y| < W/2 \\ 0, & \text{otherwise} \end{cases}. \tag{B6}$$

We again integrate Eq. (B5) over the volume $V(z_0)$ above the level $z = z_0$ to obtain a volume-integrated buoyancy budget,

$$\frac{\partial}{\partial t} \iiint_V b\, dt = -\iint_A F_b|_{z=0}\, dA + \iint_A wb|_{z=0}\, dA. \tag{B7}$$

Last, we integrate Eq. (B7) from $t = 0$ to $t = t_0$, and we obtain

$$\iiint_V b|_{t=t_0} - b|_{t=0}\, dt = -\int dx \int_{-W/2}^{W/2} B\, dy + \int_0^{t_0} dt \iint_A wb|_{z=z_0}\, dA, \tag{B8}$$

where $B = \int_0^{t_0} \dot{B}\, dt$ is the time-integrated upward surface buoyancy flux.

We will now combine Eqs. (B4) and (B8) to constrain the eddy kinetic energy. First, we use Eq. (B8) to quantify the maximum kinetic energy production that can occur at a given depth $z = z_0$. This occurs when $b|_{t=t_0} = b|_{t=0}$, that is, when the buoyancy anomalies injected at the surface of the lead have all been transported to a depth greater than z_0. This implies that

$$\int_0^{t_0} dt \iint_A wb|_{z=z_0}\, dA \lesssim BWL_x. \tag{B9}$$

Second, we substitute Eq. (B9) into Eq. (B4) to obtain an upper bound on the total kinetic energy. To obtain this bound we consider an extreme case in which Eq. (B9) holds for all depths above the base of the mixed layer; that is, all lead-injected buoyancy anomalies lie at the base of the mixed layer, $z = -H_m$. We further assume that the KE flux downward across the mixed layer base is zero and neglect the nonconservative terms. Under these assumptions, Eq. (B4) becomes

$$\iiint_V \mathrm{KE}\, dV \lesssim BWL_xH_m. \tag{B10}$$

Last, we assume that the mean component of the KE, $0.5\overline{\mathbf{u}}^2$, and the vertical eddy kinetic energy, $0.5\overline{w'^2}$, are negligible relative to the horizontal component of the eddy kinetic energy EKE. Dividing Eq. (B10) by the mixed layer depth and the domain horizontal area, we then obtain an upper bound on the horizontally averaged EKE in the mixed layer

$$\mathrm{EKE}_{\mathrm{ML}} = \frac{1}{H_m} \int_{-H_m}^{0} dz \frac{1}{L_xL_y} \iint_A \mathrm{EKE}\, dA \lesssim \frac{BW}{L_y}. \tag{B11}$$

REFERENCES

Akitomo, K., 2005: Numerical study of baroclinic instability associated with thermobaric deep convection at high latitudes: Idealized cases. *Deep-Sea Res. I*, **52**, 937–957, https://doi.org/10.1016/j.dsr.2004.12.010.

Anderson, D. L., 1961: Growth rate of sea ice. *J. Glaciol.*, **3**, 1170–1172, https://doi.org/10.1017/S0022143000017676.

Bauer, J., and S. Martin, 1983: A model of grease ice growth in small leads. *J. Geophys. Res.*, **88**, 2917–2925, https://doi.org/10.1029/JC088iC05p02917.

Bourgault, P., D. Straub, K. Duquette, L.-P. Nadeau, and B. Tremblay, 2020: Vertical heat fluxes beneath idealized sea ice leads in large-eddy simulations: Comparison with observations from the SHEBA experiment. *J. Phys. Oceanogr.*, **50**, 2189–2202, https://doi.org/10.1175/JPO-D-19-0298.1.

Bush, J. W. M., and A. W. Woods, 1999: Vortex generation by line plumes in a rotating stratified fluid. *J. Fluid Mech.*, **388**, 289–313, https://doi.org/10.1017/S0022112099004759.

——, and ——, 2000: An investigation of the link between lead-induced thermohaline convection and Arctic eddies. *Geophys. Res. Lett.*, **27**, 1179–1182, https://doi.org/10.1029/1999GL002314.

Chapman, W. L., and J. E. Walsh, 2007: A synthesis of Antarctic temperatures. *J. Climate*, **20**, 4096–4117, https://doi.org/10.1175/JCLI4236.1.

Cole, S. T., M.-L. Timmermans, J. M. Toole, R. A. Krishfield, and F. T. Thwaites, 2014: Ekman veering, internal waves, and turbulence observed under Arctic sea ice. *J. Phys. Oceanogr.*, **44**, 1306–1328, https://doi.org/10.1175/JPO-D-12-0191.1.

D'Asaro, E. A., 1988: Observations of small eddies in the Beaufort Sea. *J. Geophys. Res. Oceans*, **93**, 6669–6684, https://doi.org/10.1029/JC093iC06p06669.

Eady, E. T., 1949: Long waves and cyclone waves. *Tellus*, **1**, 33–52, https://doi.org/10.3402/tellusa.v1i3.8507.

Fox-Kemper, B., R. Ferrari, and R. Hallberg, 2008: Parameterization of mixed layer eddies. Part I: Theory and diagnosis. *J. Phys. Oceanogr.*, **38**, 1145–1165, https://doi.org/10.1175/2007JPO3792.1.

Gent, P. R., and J. C. McWilliams, 1990: Isopycnal mixing in ocean circulation models. *J. Phys. Oceanogr.*, **20**, 150–155, https://doi.org/10.1175/1520-0485(1990)020<0150:IMIOCM>2.0.CO;2.

Goosse, H., and Coauthors, 2018: Quantifying climate feedbacks in polar regions. *Nat. Commun.*, **9**, 1919, https://doi.org/10.1038/s41467-018-04173-0.

Hattermann, T., 2018: Antarctic thermocline dynamics along a narrow shelf with easterly winds. *J. Phys. Oceanogr.*, **48**, 2419–2443, https://doi.org/10.1175/JPO-D-18-0064.1.

Heorton, H. D., N. Radia, and D. L. Feltham, 2017: A model of sea ice formation in leads and polynyas. *J. Phys. Oceanogr.*, **47**, 1701–1718, https://doi.org/10.1175/JPO-D-16-0224.1.

Hibler, W. D., III, 1979: A dynamic thermodynamic sea ice model. *J. Phys. Oceanogr.*, **9**, 815–846, https://doi.org/10.1175/1520-0485(1979)009<0815:ADTSIM>2.0.CO;2.

Holland, P. R., and R. Kwok, 2012: Wind-driven trends in Antarctic sea-ice drift. *Nat. Geosci.*, **5**, 872–875, https://doi.org/10.1038/ngeo1627.

Holte, J., and L. Talley, 2009: A new algorithm for finding mixed layer depths with applications to Argo data and Subantarctic Mode Water formation. *J. Atmos. Oceanic Technol.*, **26**, 1920–1939, https://doi.org/10.1175/2009JTECHO543.1.

Jackett, D. R., and T. J. McDougall, 1995: Minimal adjustment of hydrographic profiles to achieve static stability. *J. Atmos. Oceanic Technol.*, **12**, 381–389, https://doi.org/10.1175/1520-0426(1995)012<0381:MAOHPT>2.0.CO;2.

Jansen, M. F., A. J. Adcroft, R. Hallberg, and I. M. Held, 2015: Parameterization of eddy fluxes based on a mesoscale energy budget. *Ocean Modell.*, **92**, 28–41, https://doi.org/10.1016/j.ocemod.2015.05.007.

Kantha, L. H., 1995: A numerical model of arctic leads. *J. Geophys. Res.*, **100**, 4653–4672, https://doi.org/10.1029/94JC02348.

Key, J., R. Stone, J. Maslanik, and E. Ellefsen, 1993: The detectability of sea-ice leads in satellite data as a function of atmospheric conditions and measurement scale. *Ann. Glaciol.*, **17**, 227–232, https://doi.org/10.3189/S026030550001288X.

LaCasce, J.-H., 2008: Statistics from Lagrangian observations. *Prog. Oceanogr.*, **77**, 1–29, https://doi.org/10.1016/j.pocean.2008.02.002.

LaCasce, J., R. Ferrari, J. Marshall, R. Tulloch, D. Balwada, and K. Speer, 2014: Float-derived isopycnal diffusivities in the DIMES experiment. *J. Phys. Oceanogr.*, **44**, 764–780, https://doi.org/10.1175/JPO-D-13-0175.1.

Larichev, V. D., and I. M. Held, 1995: Eddy amplitudes and fluxes in a homogeneous model of fully developed baroclinic instability. *J. Phys. Oceanogr.*, **25**, 2285–2297, https://doi.org/10.1175/1520-0485(1995)025<2285:EAAFIA>2.0.CO;2.

Lindsay, R. W., and D. A. Rothrock, 1995: Arctic sea ice leads from advanced very high resolution radiometer images. *J. Geophys. Res.*, **100**, 4533–4544, https://doi.org/10.1029/94JC02393.

Manley, T. O., and K. Hunkins, 1985: Mesoscale eddies of the Arctic Ocean. *J. Geophys. Res.*, **90**, 4911–4930, https://doi.org/10.1029/JC090iC03p04911.

Manucharyan, G. E., and M.-L. Timmermans., 2013: Generation and separation of mesoscale eddies from surface ocean fronts. *J. Phys. Oceanogr.*, **43**, 2545–2562, https://doi.org/10.1175/JPO-D-13-094.1.

Marshall, J., and F. Schott, 1999: Open-ocean convection: Observations, theory, and models. *Rev. Geophys.*, **37**, 1–64, https://doi.org/10.1029/98RG02739.

——, A. Adcroft, C. Hill, L. Perelman, and C. Heisey, 1997a: A finite-volume, incompressible Navier Stokes model for studies of the ocean on parallel computers. *J. Geophys. Res.*, **102**, 5753–5766, https://doi.org/10.1029/96JC02775.

——, C. Hill, L. Perelman, and A. Adcroft, 1997b: Hydrostatic, quasi-hydrostatic, and nonhydrostatic ocean modeling. *J. Geophys. Res.*, **102**, 5733–5752, https://doi.org/10.1029/96JC02776.

Matsumura, Y., and H. Hasumi, 2008: Brine-driven eddies under sea ice leads and their impact on the Arctic Ocean mixed layer. *J. Phys. Oceanogr.*, **38**, 146–163, https://doi.org/10.1175/2007JPO3620.1.

McDougall, T. J., and P. M. Barker, 2011: Getting started with TEOS-10 and the Gibbs Seawater (GSW) Oceanographic Toolbox. SCOR/IAPSO WG127, 28 pp., http://www.teos-10.org/pubs/Getting_Started.pdf.

McPhee, M. G., 2012: Advances in understanding ice–ocean stress during and since AIDJEX. *Cold Reg. Sci. Technol.*, **76–77**, 24–36, https://doi.org/10.1016/j.coldregions.2011.05.001.

Meneghello, G., J. Marshall, C. Lique, P. E. Isachsen, E. Doddridge, J.-M. Campin, H. Regan, and C. Talandier, 2021: Genesis and decay of mesoscale baroclinic eddies in the seasonally ice-covered interior Arctic Ocean. *J. Phys. Oceanogr.*, **51**, 115–129, https://doi.org/10.1175/JPO-D-20-0054.1.

Millero, F. J., and W. Leung, 1976: Thermodynamics of seawater at one atmosphere. *Am. J. Sci.*, **276**, 1035–1077, https://doi.org/10.2475/ajs.276.9.1035.

Morison, J. H., M. G. McPhee, T. B. Curtin, and C. A. Paulson, 1992: The oceanography of winter leads. *J. Geophys. Res.*, **97**, 11 199–11 218, https://doi.org/10.1029/92JC00684.

Muench, R. D., J. T. Gunn, T. E. Whitledge, P. Schlosser, and W. Smethie Jr., 2000: An Arctic Ocean cold core eddy. *J. Geophys. Res.*, **105**, 232997–242006, https://doi.org/10.1029/2000JC000212.

Naveira Garabato, A. C., E. L. McDonagh, D. P. Stevens, K. J. Heywood, and R. J. Sanders, 2002: On the export of Antarctic bottom water from the Weddell Sea. *Deep-Sea Res. II*, **49**, 4715–4742, https://doi.org/10.1016/S0967-0645(02)00156-X.

Nguyen, A. T., D. Menemenlis, and R. Kwok, 2009: Improved modeling of the Arctic halocline with a subgrid-scale brine rejection parameterization. *J. Geophys. Res.*, **114**, C11014, https://doi.org/10.1029/2008JC005121.

Ohshima, K., Y. Fukamachi, and G. Williams, 2013: Antarctic Bottom Water production by intense sea-ice formation in the Cape Darnley polynya. *Nat. Geosci.*, **6**, 235–240, https://doi.org/10.1038/ngeo1738.

Park, H.-S., and A. Stewart, 2016: An analytical model for wind-driven arctic summer sea ice drift. *Cryosphere*, **10**, 227–244, https://doi.org/10.5194/tc-10-227-2016.

Pellichero, V., J.-B. Sallée, S. Schmidtko, F. Roquet, J.-B. Charrassin, 2017: The ocean mixed layer under Southern Ocean sea-ice: Seasonal cycle and forcing. *J. Geophys. Res. Oceans*, **122**, 1608–1633, https://doi.org/10.1002/2016JC011970.

Pickart, R. S., T. S. Weingartner, L. J. Pratt, S. Zimmermann, and D. J. Torres, 2005: Flow of winter-transformed Pacific water into the western Arctic. *Deep-Sea Res. II*, **52**, 3175–3198, https://doi.org/10.1016/j.dsr2.2005.10.009.

Prandtl, L., 1925: Bericht Über Untersuchungen zur ausgebildeten Turbulenz. *Zeitschr. Angew. Math. Mech.*, **5**, 136–139, https://doi.org/10.1002/zamm.19250050212.

Reiser, F., S. Willmes, and G. Heinemann, 2020: A new algorithm for daily sea ice lead identification in the Arctic and Antarctic winter from thermal-infrared satellite imagery. *Remote Sens.*, **12**, 1957, https://doi.org/10.3390/rs12121957.

Rocha, C. B., T. K. Chereskin, S. T. Gille, and D. Menemenlis, 2016: Mesoscale to submesoscale wavenumber spectra in Drake Passage. *J. Phys. Oceanogr.*, **46**, 601–620, https://doi.org/10.1175/JPO-D-15-0087.1.

Semtner, A. J., 1976: A model for the thermodynamic growth of sea ice in numerical investigations of climate. *J. Phys. Oceanogr.*, **6**, 379–389, https://doi.org/10.1175/1520-0485(1976)006<0379:AMFTTG>2.0.CO;2.

Send, U., and J. Marshall, 1995: Integral effects of deep convection. *J. Phys. Oceanogr.*, **25**, 855–872, https://doi.org/10.1175/1520-0485(1995)025<0855:IEODC>2.0.CO;2.

Skyllingstad, E. D., and D. W. Denbo, 2001: Turbulence beneath sea ice and leads: A coupled sea ice/large-eddy simulation study. *J. Geophys. Res.*, **106**, 2477–2497, https://doi.org/10.1029/1999JC000091.

Smith, D. C., and J. H. Morison, 1998: Nonhydrostatic haline convection under leads in sea ice. *J. Geophys. Res.*, **103**, 3233–3247, https://doi.org/10.1029/97JC02262.

——, J. W. Lavelle, and H. J. S. Fernando, 2002: Arctic Ocean mixed-layer eddy generation under leads in sea ice. *J. Geophys. Res.*, **107**, 3103, https://doi.org/10.1029/2001JC000822.

Smith, S. D., R. D. Muench, and C. H. Pease, 1990: Polynyas and leads: An overview of physical processes and environment. *J. Geophys. Res.*, **95**, 9461–9479, https://doi.org/10.1029/JC095iC06p09461.

Steiner, N., and Coauthors, 2004: Comparing modeled streamfunction, heat and freshwater content in the Arctic Ocean. *Ocean Modell.*, **6**, 265–284, https://doi.org/10.1016/S1463-5003(03)00013-1.

Stewart, A. L., A. Klocker, and D. Menemenlis, 2018: Circum-Antarctic shoreward heat transport derived from an eddy-and tide-resolving simulation. *Geophys. Res. Lett.*, **45**, 834–845, https://doi.org/10.1002/2017GL075677.

——, ——, and ——, 2019: Acceleration and overturning of the Antarctic slope currents by winds, eddies and tides. *J. Phys. Oceanogr.*, **49**, 2043–2074, https://doi.org/10.1175/JPO-D-18-0221.1.

Tarshish, N., R. Abernathey, C. Zhang, C. O. Dufour, I. Frenger, and S. M. Griffies, 2018: Identifying Lagrangian coherent vortices in a mesoscale ocean model. *Ocean Modell.*, **130**, 15–28, https://doi.org/10.1016/j.ocemod.2018.07.001.

Thompson, A. F., and W. R. Young, 2006: Scaling baroclinic eddy fluxes: Vortices and energy balance. *J. Phys. Oceanogr.*, **36**, 720–738, https://doi.org/10.1175/JPO2874.1.

Timmermans, M.-L., and J. Marshall, 2020: Understanding Arctic Ocean circulation: A review of Ocean dynamics in a changing climate. *J. Geophys. Res. Oceans*, **125**, e2018JC014378, https://doi.org/10.1029/2018JC014378.

——, J. Toole, A. Proshutinsky, R. Krishfield, and A. Plueddemann, 2008: Eddies in the Canada Basin, Arctic Ocean, observed from ice-tethered profilers. *J. Phys. Oceanogr.*, **38**, 133–145, https://doi.org/10.1175/2007JPO3782.1.

Towns, J., and Coauthors, 2014: XSEDE: Accelerating scientific discovery. *Comput. Sci. Eng.*, **16**, 62–74, https://doi.org/10.1109/MCSE.2014.80.

Turner, J., and Coauthors, 2005: Antarctic climate change during the last 50 years. *Int. J. Climatol.*, **25**, 279–294, https://doi.org/10.1002/joc.1130.

Vallis, G. K., 2006: *Atmospheric and Oceanic Fluid Dynamics*. Cambridge University Press, 745 pp.

Visbeck, M., J. Marshall, T. Haine, and M. Spall, 1997: Specification of eddy transfer coefficients in coarse-resolution ocean circulation models. *J. Phys. Oceanogr.*, **27**, 381–402, https://doi.org/10.1175/1520-0485(1997)027<0381:SOETCI>2.0.CO;2.

Wadhams, P., A. S. McLaren, and R. Weintraub, 1985: Ice thickness distribution in Davis Straight in February from submarine Sonar Profiles. *J. Geophys. Res.*, **90**, 1069–1077, https://doi.org/10.1029/JC090iC01p01069.

Wang, Y., and A. L. Stewart, 2020: Scalings for eddy buoyancy transfer across continental slopes under retrograde winds. *Ocean Modell.*, **147**, 101579, https://doi.org/10.1016/j.ocemod.2020.101579.

——, F. J. Beron-Vera, and M. J. Olascoaga, 2016: The life cycle of a coherent Lagrangian Agulhas ring. *J. Geophys. Res. Oceans*, **121**, 3944–3954, https://doi.org/10.1002/2015JC011620.

Wilchinsky, A. V., H. D. Heorton, D. L. Feltham, and P. R. Holland, 2015: Study of the impact of ice formation in leads upon the sea ice pack mass balance using a new frazil and grease ice parameterization. *J. Phys. Oceanogr.*, **45**, 2025–2047, https://doi.org/10.1175/JPO-D-14-0184.1.

Winters, K. B., P. N. Lombard, J. J. Riley, and E. A. D'Asaro, 1995: Available potential energy and mixing in density-stratified fluids. *J. Fluid Mech.*, **289**, 115–128, https://doi.org/10.1017/S002211209500125X.

Zhao, M., M.-L. Timmermans, S. Cole, R. Krishfield, A. Proshutinsky, and J. Toole, 2014: Characterizing the eddy field in the Arctic Ocean halocline. *J. Geophys. Res. Oceans*, **119**, 8800–8817, https://doi.org/10.1002/2014JC010488.

——, ——, ——, ——, and J. Toole, 2016: Evolution of the eddy field in the Arctic Ocean's Canada Basin, 2005–2015. *Geophys. Res. Lett.*, **43**, 8106–8114, https://doi.org/10.1002/2016GL069671.